Self-consistent Maxwell-Bloch model of quantum-dot photonic-crystal-cavity lasers

William Cartar,[1] Jesper Mørk,[2] and Stephen Hughes[1]

[1]*Department of Physics, Engineering Physics and Astronomy, Queen's University, Kingston, Ontario, Canada K7L 3N6*
[2]*DTU Fotonik, Department of Photonics Engineering, Technical University of Denmark, Building 345W, 2800 Kgs. Lyngby, Denmark*

We present a powerful computational approach to simulate the threshold behavior of photonic-crystal quantum-dot (QD) lasers. Using a finite-difference time-domain (FDTD) technique, Maxwell-Bloch equations representing a system of thousands of statistically independent and randomly positioned two-level emitters are solved numerically. Phenomenological pure dephasing and incoherent pumping is added to the optical Bloch equations to allow for a dynamical lasing regime, but the cavity-mediated radiative dynamics and gain coupling of each QD dipole (artificial atom) is contained self-consistently within the model. These Maxwell-Bloch equations are implemented by using Lumerical's flexible material plug-in tool, which allows a user to define additional equations of motion for the nonlinear polarization. We implement the gain ensemble within triangular-lattice photonic-crystal cavities of various length N (where N refers to the number of missing holes), and investigate the cavity mode characteristics and the threshold regime as a function of cavity length. We develop effective two-dimensional model simulations which are derived after studying the full three-dimensional passive material structures by matching the cavity quality factors and resonance properties. We also demonstrate how to obtain the correct point-dipole radiative decay rate from Fermi's golden rule, which is captured naturally by the FDTD method. Our numerical simulations predict that the pump threshold plateaus around cavity lengths greater than $N = 9$, which we identify as a consequence of the complex spatial dynamics and gain coupling from the inhomogeneous QD ensemble. This behavior is not expected from simple rate-equation analysis commonly adopted in the literature, but is in qualitative agreement with recent experiments. Single-mode to multimode lasing is also observed, depending on the spectral peak frequency of the QD ensemble. Using a statistical modal analysis of the average decay rates, we also show how the average radiative decay rate decreases as a function of cavity size. In addition, we investigate the role of structural disorder on both the passive cavity and active lasers, where the latter show a general increase in the pump threshold for cavity lengths greater than $N = 7$, and a reduction in the nominal cavity mode volume for increasing amounts of disorder.

I. INTRODUCTION

Microcavity photonic crystals (PCs) are a natural advancement to mirror-based feedback systems as many technologies shrink to the nanoscale. The vertical cavity surface emitting laser (VCSEL) was successfully demonstrated in 1989 [1], and has found applications in telecommunication systems, optical interconnects, spectroscopic sensing, and optical image processing. In 1994, Dowling *et al.* proposed a one-dimensional (1D) PC operating near the photonic band edge [2], making use of slow-light modes to increase the power emitted by such lasers, which has been one of the limitations of microcavity lasers [3]. Experimentally, slow-light band edge lasers have now been demonstrated in both two-dimensional (2D) [4–12] and three-dimensional (3D) [13–15] architectures, while over the past decade, significant progress has been made in the optimization of these lasers [15–18], allowing for the investigation of new operation regimes such as single emitter lasing [19], ultrahigh speed modulation [20], and self-pulsing [21]. To directly model the optical properties of open-system microcavity structures, finite-difference time-domain (FDTD) techniques are often employed since such open cavities support quasinormal modes (QNMs) that have a finite lifetime due their coupling to a continuum of modes with outgoing boundary conditions [22]. For example, quasinormal modes are obtained from the mode solutions to the Helmholz equation with open boundary conditions [23], resulting in a complex

eigenfrequency for each cavity mode. To numerically model a gain medium within the cavity, various techniques have been implemented ranging from the simple inclusion of a negative imaginary component in the refractive index [24] to including rate equations embedded in the FDTD algorithm [3,25,26], or with the finite element method [27]. It is also common to adopt simple rate equations for the population density of carriers and photon flux [28,29], which can quickly connect to experimental data. It is, however, still a major challenge to model arbitrarily shaped gain materials coupled to arbitrarily shaped cavity structures, which is desired for many quantum-dot (QD) microcavity structures, especially as the modal properties of the laser cavity change drastically as a function of position and size (which results in spatially dependent radiative coupling and gain dynamics). Semiconductor QDs are now increasingly used as the underlying gain material in microcavity lasers, due to their superior room-temperature operation [30], tunability [31], unique atomlike density of states and carrier dynamics [32], and excellent temporal and spatial stability [30,33]. To develop a theoretical model of the light-matter interactions, one approach is to model their collective gain more appropriately as an ensemble of effective two-level atoms (TLAs) [34–36].

The simplest implementation of a TLA coupled to electromagnetic fields is achieved with the optical Bloch equations (OBEs), which adds appropriate linear and nonlinear interactions between the dipole-induced polarization and electric

field, giving rise to the Maxwell-Bloch (MB) equations when combined with the Maxwell equations [37]. Using an effective TLA, positive population inversion can be achieved, e.g., by a phenomenological incoherent pump rate that mimics ultrafast relaxation rates from higher-lying levels to the lasing exciton state, thus eliminating the need for additional energy levels. This simple model of an artificial atom, implemented with Maxwell's equations, has the distinct benefit of allowing one to study general light-matter interactions without using either of the rotating-wave approximation or the slowly-varying-envelope approximation, which have already led to a wide range of new effects such as the dynamic nonlinear skin effect [38] and carrier-wave Rabi flopping [39,40], even with simple 1D equations of motion. Moreover, when studying quantum information systems that are dominated by radiative decay, it is critical to preserve the coherent radiative contributions that a MB analysis provides [41], without recourse to adding in phenomenological damping constants. Otherwise, if non-radiative processes dominate, a more straightforward MB formalism may be used, in which phenomenological damping terms like pure dephasing are implemented [42,43]. Direct MB simulations have been successfully used for a number of years. For example, Anderson and Cao used a 1D FDTD scheme to simulate stochastic noise in macroscopic atomic systems [44]; Andreasen *et al.* carried out FDTD simulation of thermal noise in open cavities [45]; while Sukharev studied the interaction of chirped femtosecond laser pulses with hybrid materials comprised of plasmon grating structures and resonant molecules [46].

In many nanophotonic cavity structures, it is critical to go beyond the 1D models and the commonly adopted simple rate equations; e.g., Sukharev and Nitzan have studied atomic samples interacting with materials using a 2D MB model [47]; Pusch *et al.* studied amplification and noise in gain-enhanced plasmonic materials using a 3D model [48]; Lopata and Neuhauser [49] studied the effect of nonlinear excitations of a dipolar molecule on plasmon transfer across a pair of spherical gold nanoparticles using a split-field FDTD-Schrödinger approach; Gray and Kupka [50] carried out FDTD studies of a variety of silver cylinder arrays with nanometer-scale diameters (nanowires) interacting with light; and Dridi and Schatz [51] introduced a model for describing plasmon-enhanced lasers that combines rate equations with FDTD for describing plasmon-enhanced lasers. Many of the radiative decay processes are also affected by unavoidable fabrication disorder, and even minute (nm-scale) levels of disorder can play an important role in understanding the rich physics of slow-light systems [52–58]. Deliberate disorder can be added to a system to gain access to novel effects such as reduced laser thresholds in random laser systems [24], brought on by Anderson localization [59]. Indeed, there is continued interest in understanding Anderson localization modes and random lasing [60–62], which has recently been studied in various disordered PC waveguide systems [56,58,63].

With the current trend of miniaturized semiconductor laser systems, there is now a need for more sophisticated models of PC lasers beyond the simple rate-equation picture [28,64], where the emitters' coherence is assumed to be in steady state or adiabatically eliminated, leading to coupled equations between the available energy levels without any information
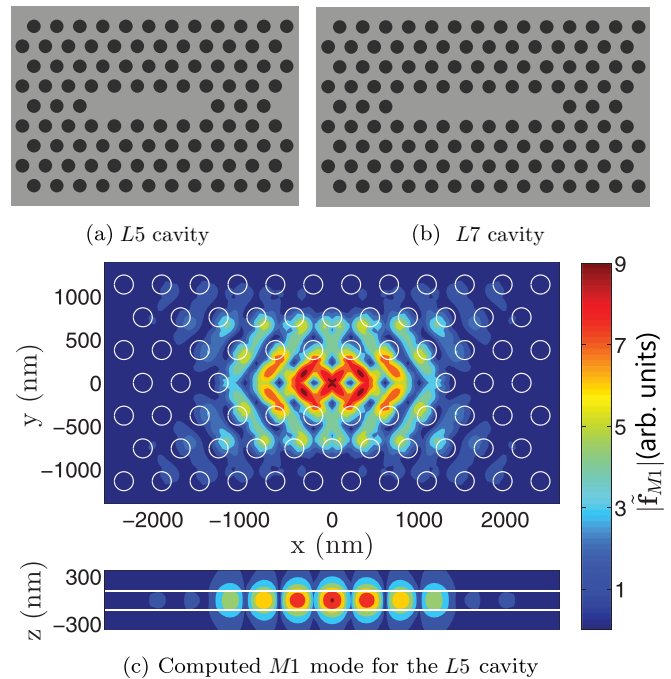

(a) *L*5 cavity (b) *L*7 cavity

(c) Computed *M*1 mode for the *L*5 cavity

FIG. 1. Top-down view region of an *L*5 (a) and *L*7 (b) PC slab cavity. (c) First fundamental mode (*M*1) profile $|\mathbf{E}(\mathbf{r})|$, inside an *L*5 cavity, computed by 3D FDTD simulations. The circle outlines where etched holes exist within the homogeneous background material, which has an index of refraction of $n = 3.17$ in 3D simulations. The two white lines in the $x - z$ spatial profile represent the characteristic length $l_{z,V}$ we use to relate 2D mode volumes to 3D calculations (see Sec. II). The slab has lattice pitch $a = 438$ nm, radius $r = a/4$, and height $h = 250$ nm. The mode profile measured at the center of the 3D slabs (in the z direction) is very similar to an effective 2D mode profile with the same properties, except $n = 2.54$ (see text).

regarding the system coherence. In many cases, this may fail to describe emerging experiments. For example, a recent investigation of lasing threshold as a function of band-edge proximity, performed by increasing a triangular lattice PC cavity length, found counterintuitive results [13]: rather than a decreasing gain threshold for increasing cavity length, which is predicted by simple laser theory, there existed a threshold minimum around the *L*8-*L*9 cavity length scale, where *LN* denotes a cavity of length *N* (missing holes in the lattice), and cavity lengths ranging from *L*3–*L*20 were created. Two example schematics are shown in in Figs. 1(a) and 1(b). These cavities have fundamental cavity modes (*M*1, *M*2, ...) confined within the cavity region, as shown in Fig. 1(c) for an *L*5 cavity. In the theoretical analysis of a 2D square-based PC microcavity laser, a similar trend is observed, but only for systems with low optical density of states (DOS) [3]. Since the DOS and LDOS (local DOS) of band-edge cavities are so high, the results of Ref. [13] were partly explained by a heuristic model of disorder-induced backscattering and outscattering of the Bloch mode into modes above the light line (which is known to occur in longer-length PC waveguides). In such a model, disorder shifts some of the lasing mode near the band edge into the regime where it is no longer confined to the cavity structure, and this shift is felt more strongly by

longer cavity modes (slower light is more sensitive to disorder), which exist deeper in the slow-light regime, thus creating an optimal pump threshold by minimizing both reflection losses and backscattering losses.

In this paper, we present a systematic numerical study of a QD ensemble in triangular-lattice PC cavities, and explore the lasing threshold behavior as a function of PC length. We closely follow the designs and recent experiments of Xue *et al.* [13], and also partly explore the role of structural disorder on the lasing threshold in PC cavities, which were credited to be likely responsible for the unusual gain threshold dependence on cavity length. Using Lumerical's FDTD material plug-in tool, which allows a user to include unique polarizations in simulation objects [65], we investigate the gain and lasing behavior of effective 2D cavity laser structures, modeled after full 3D passive simulations. Although we use Lumerical FDTD, the general technique can naturally be adopted with any general FDTD (or time-dependent Maxwell) solver. The user-controlled plug-in tool returns MB dynamics by solving the OBEs (for each QD), and includes radiative decay, local gain, and inter-QD coupling that is fully captured self-consistently by the FDTD method, as well as pure dephasing included as a phenomenological decay rate, and an incoherent pump term which effectively models a three-level gain system for each QD. The OBE plug-in has the distinct advantage of being completely general, solving lasing dynamics and gain coupling with zero *a priori knowledge* (other than inherent properties of the QDs), when compared to traditional rate equations [28,29], and they easily capture the statistical behavior of a QD ensemble as well.

The remainder of our paper is organized as follows: In Sec. II, we introduce the cavity parameters and model the basic cavity properties of the 2D simulations after obtaining the results for passive 3D (slab) structures. In addition, we investigate the role of fabrication disorder of the PC lattice, and model 2D after 3D simulations once more. In Sec. III, we introduce our model OBEs, and discuss their implementation within the plug-in tool as a source for nonlinear polarization. In Sec. IV, we discuss the dipole moment used in our simulations and explain how to obtain the correct 3D radiative decay of a point dipole in an effective 2D model. In Sec. V, we discuss the implementation of QDs in the FDTD method, and model our radiative decay after 3D simulations. In Sec. VI, we outline and discuss the results of including an active QD ensemble (including 14 000–24 000 randomly positioned QDs with random center frequencies) for various cavity lengths, extracting pump thresholds, and investigating different models of the plug in. We connect our results to the recent experiments of Xue *et al.* [13] and standard rate equations, and provide insights into the gain threshold dependence on cavity length. We summarize in Sec. VII. In the Appendix, we exemplify the role of structural disorder on the gain threshold and lasing modes, and highlight a number of effects such as mode localization for increasing disorder.

II. PASSIVE CAVITY SIMULATIONS: EFFECTIVE 2D SIMULATIONS AND ROLE OF FABRICATION DISORDER

Full 3D simulations of passive PC slab structures (i.e., with no gain material) form an appropriate starting point to model
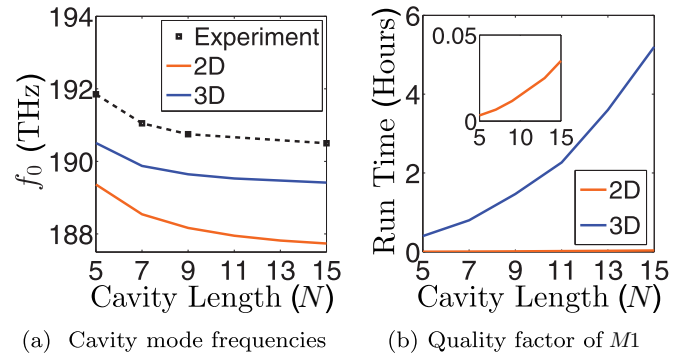

(a) Cavity mode frequencies   (b) Quality factor of $M1$

FIG. 2. Passive cavity simulations for an LN cavity in a triangular PC cavity with lattice pitch $a = 438$ nm, radius $r = a/4$, height $h = 250$ nm (in 3D), and refractive index $n = 3.17$ or 2.54 for 3D and 2D simulations, respectively. (a) Comparison of the fundamental mode's peak frequency as a function of cavity length, for 2D and 3D simulations, with experimental data points from 13 for reference. (b) Run-time requirements using 16 cores with 1024 Mb of memory, for a single passive 2D or 3D simulation, without QD mesh requirements, as a function of cavity length (see text).

planar PC slabs with no active QDs, as they produce the main mode characteristics and allow for additional key parameters such as Q, V_{eff}, and local density of states (LDOS). However, 2D simulations take significantly less time to run, and can be modeled after 3D simulations to capture the key properties of PC slab modes with similar peak properties, such as mode frequency [shown in Fig. 2(a)] and Q factors (studied later), at a fraction of the computational cost [see Fig. 2(b)]. This is important for developing effective 2D models for the full Maxwell OBEs with gain materials and many thousands of OBEs (i.e., one OBE set for each QD). It should also be noted that Fig. 2(b) is obtained for passive structures only, and to accurately include QD dipoles in our simulation, we require a finer spatial mesh of more than twice what is typically used in passive simulations. As such, the simulations performed with a QD ensemble require significantly longer to run than is represented in Fig. 2(b), so that the lasing dynamics may eventually reach steady state (SS). For example, each of our 2D $L15$ lasing simulations (shown below) takes roughly 20 hours to run, when 16 computational cores are used with 1024 Mb of memory each. This increased run time is roughly 400 times the passive simulations shown in Fig. 2(b). As such, for this first study, we chose to develop an effective 2D FDTD method when using the OBEs, which makes it easier to carry out a systematic sweep of various system parameters such as cavity length and pump powers, especially important for high-Q cavity modes which take a long time to reach SS.

In order to introduce an accurate effective 2D cavity simulation, similar to the PC cavity experiments of Xue *et al.* [13], we first capture the basic cavity physics using passive 3D slab simulations. The cavities are assumed to be made of InP, with a standard hexagonal lattice PC cavity, without any hole shifts or modifications to optimize the cavity Q. The lattice pitch is $a = 438$ nm, with hole radius $r = a/4$, slab height $h = 250$ nm, and refractive index $n = 3.17$ [13]. The PC band gap (TE-like) is roughly 185–215 THz, and the QDs have parameters similar to InAs. Our simulations are run

(a) $M1$ Q with and without structural disorder

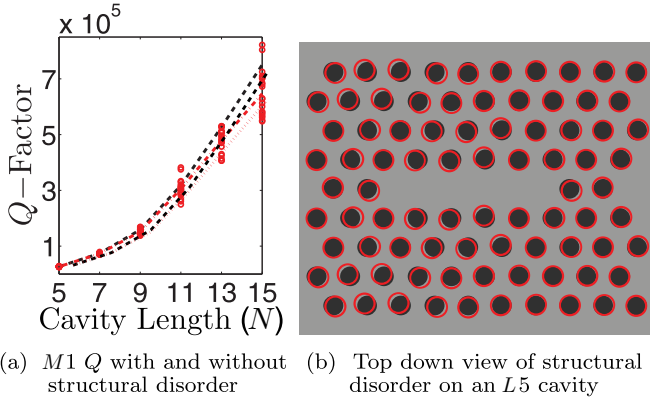(b) Top down view of structural disorder on an $L5$ cavity

FIG. 3. (a) Impact of intrinsic levels of structural disorder (red circles) on 3D FDTD PC cavity simulations as a function of cavity length, averaged over 20 instances (red dotted-dashed line), compared to ordered simulations (dashed black line). (b) Schematic top view of the disordered cavity simulation with the disordered holes (red circles) over-top the ideal air holes (black holes), and the background slab (gray); this is a zoom-in region and in the simulations use a larger domain seen in Fig. 5(b).

using Lumerical's [65] FDTD software, with open boundary conditions via perfectly matched layers (PMLs).

An example of the $L5$ cavity is displayed in Figs. 1(c) and 3(b). We simulate cavity lengths ranging from $L5$–$L15$ skipping even cavity lengths, and measuring the resulting Q factors for all fundamental modes observed in the simulations. The cavity modes are excited by a dipole source defined by a fixed carrier frequency with a temporal Gaussian envelope, located along the center axis of the cavity, shifted from the central y axis to avoid emitting at the antinode points of even cavity modes (i.e., $M2$, $M4$, etc.). To capture the modal properties of each cavity, two simulations are run; the first simulation uses an electric-field time monitor to measure the first few dominant mode eigenfrequencies $\tilde{\omega}_\mu = \omega_\mu - i\Gamma_\mu$, where ω_μ is the peak frequency, and $\Gamma_\mu = \frac{\omega_\mu}{2Q_\mu}$ is defined by the mode broadening and the cavity quality factor Q; the second simulation measures each mode's spatial QNM profile $\tilde{\mathbf{f}}(\mathbf{r})$ using a discrete Fourier transform (DFT) monitor. Typically, three–five modes are measured in the frequency range of interest, depending on the cavity length, as longer cavities have stronger higher-order modes, and more frequencies within the simulation bandwidth.

Using the cavity mode profiles and their corresponding eigenfrequencies, we can calculate the cavity Green function (GF) using a QNM expansion [66]

$$\mathbf{G}(\mathbf{r},\mathbf{r}';\omega) = \sum_\mu \frac{\omega^2 \tilde{\mathbf{f}}_\mu(\mathbf{r})\tilde{\mathbf{f}}_\mu(\mathbf{r}')}{2\tilde{\omega}_\mu(\tilde{\omega}_\mu - \omega)}, \tag{1}$$

where μ uniquely identifies each mode, and the modes are normalized by [67]

$$\langle\langle \tilde{\mathbf{f}}_\mu | \tilde{\mathbf{f}}_\mu \rangle\rangle = \lim_{V\to\infty} \int_V \epsilon_r(\mathbf{r})\tilde{\mathbf{f}}_\mu(\mathbf{r}) \cdot \tilde{\mathbf{f}}_\mu(\mathbf{r})d\mathbf{r}$$
$$+ i\frac{c}{2\tilde{\omega}_\mu}\int_{\partial V}\sqrt{\epsilon_r(\mathbf{r})}\tilde{\mathbf{f}}_\mu(\mathbf{r}) \cdot \tilde{\mathbf{f}}_\mu(\mathbf{r})d\mathbf{r} = 1, \tag{2}$$

where $\epsilon_r(\mathbf{r})$ is the relative permittivity of the cavity, and ∂V denotes the border of volume V, in the appropriate limit [68]. With the normalized modes, we are able to calculate accurate effective mode volumes [67], which are defined from

$$V_{\text{eff}}^{-1} = \text{Re}\left\{ \frac{\epsilon_r(\mathbf{r}_c)\tilde{\mathbf{f}}_c^2(\mathbf{r}_c)}{\langle\langle \mathbf{f}_c | \mathbf{f}_c \rangle\rangle} \right\}, \tag{3}$$

where $\mathbf{r}_c$ is an antinode point of interest within the cavity structure. Having the GF defined at all locations of $\mathbf{r}$ and $\mathbf{r}'$ allows us to, e.g., plot the LDOS at any location (i.e., without having to do further dipole calculations), and normalizing by the free-space GF defines the projected LDOS to have units equivalent to the Purcell factor (PF), defined as [69]

$$\text{PF} = \frac{3}{4\pi^2}\left(\frac{\lambda}{n}\right)^3 \frac{Q}{V_{\text{eff}}}, \tag{4}$$

where λ is the wavelength and the Q is for the resonant mode of interest. This expression characterizes the enhanced radiative decay with respect to a homogeneous medium and assumes a dipole in resonance with a single cavity mode and perfectly matched to the field maximum and polarization. Furthermore, if the dipole is exposed to pure dephasing, the expression assumes that the dephasing rate is much smaller than the cavity decay rate (which we note is not the case for the simulation studies later) [64].

Next, to identify the role of fabrication or structural disorder on the passive 3D structures, we model intrinsic fabrication disorder by shifting the center of each hole by a random amount Δr characterized by the standard deviation σ_{Dis} of a random number generator. The direction of each hole's shift is also randomized, by defining a random number between $[-\pi,\pi]$, thus giving equal probability for a shift in any direction. Figure 3(b) depicts an exaggerated disorder instance for an $L5$ cavity. The required numerical size of the PC (to mimic an infinite PC system) was determined by increasing the simulation's spatial size until the largest (dominant) Q-factor value converged, and the simulation size increased as the cavity length increased to prevent spurious Q-factor measurements. The intrinsic disorder is set to be $\sigma_{\text{Dis}} = 0.005a$, as determined from related experimental far-field intensity spectra compared to FDTD simulated spectra for varying amounts of disorder [70]. Figure 3(a) depicts the measured Q factors of 20 instances of disorder at each cavity length, showing the impact of disorder is very minimal at smaller cavity lengths, and impacts the $L15$ Q factor by only about 15%. These disordered statistics are consistent with the other findings of similar PC cavity investigations [71], for the same range of Q.

Given the measured eigenfrequencies and (effective) mode volumes for passive 3D simulations, effective 2D simulations are subsequently optimized to closely match the Q factor, mode volume, and peak frequency trends of the full 3D simulations. First, the 2D simulations use an effective refractive index of $n = 2.54$ to shift the peak frequencies to match the 3D simulations, which use $n = 3.17$. Fitting this effective refractive index optimized both the location and separation between the first and second fundamental modes $M1$ and $M2$, respectively, so that any mode coupling affects would be representative of their 3D counterparts. This is mainly why Fig. 2(a) is not simply an optimized overlap between 2D and
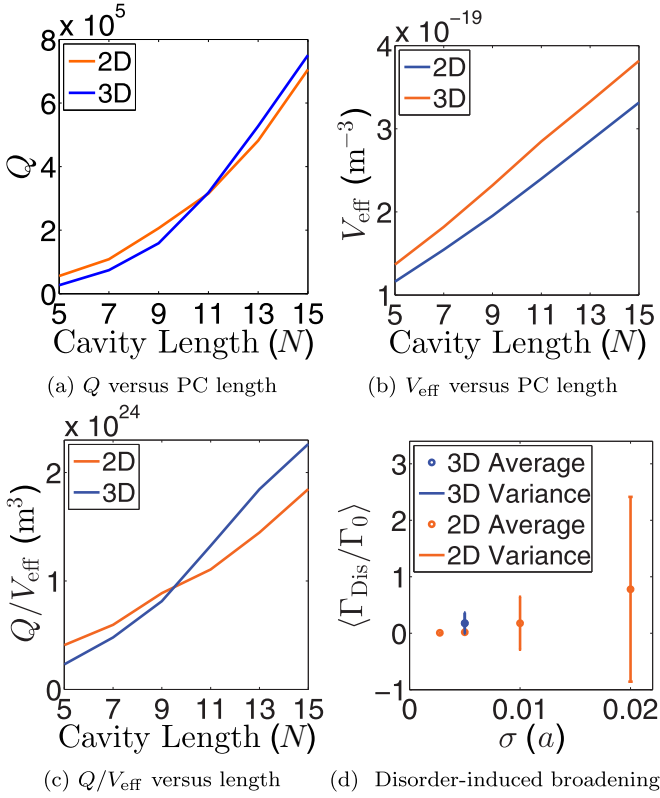
(a) Q versus PC length

(b) V_{eff} versus PC length

(c) Q/V_{eff} versus length

(d) Disorder-induced broadening

FIG. 4. (a)–(c) Q and V_{eff} modeling of effective 2D system compared to full 3D simulations, without disorder. (d) Disorder statistics of $\Gamma_{\mathrm{Dis}} = \Gamma - \Gamma_0$, for the $L15$ cavities of varying amounts of 2D disorder, referenced to the 3D intrinsic disorder of $\sigma_{\mathrm{Dis}} = 0.005a$.

3D simulation trends. In addition, to account for the leakage that occurs in 3D simulations (in that case through vertical decay), the size of the 2D PC in the x direction was set to allow cavity decay that was similar to the 3D leakage. This can be seen in Fig. 4(a), where the 2D and 3D Q factors are compared. In Fig. 4(b), we also compare 2D and 3D mode volumes, which requires a characteristic length scale $l_{z,V}$ to convert the 2D mode area $A_{\mathrm{eff,2D}}$ into a volume $V_{\mathrm{eff,2D}} = l_{z,V} A_{\mathrm{eff,2D}}$. This length scale is chosen to be 205 nm [see Fig. 1(c) in Sec. I], which is slightly less than the height of the 3D PC cavities. We chose this length scale as it gives a reasonable Q/V_{eff} fit, as shown in Fig. 4(c), while also containing the majority of the 3D mode volume (more than 85%). Given the complexity of the calculations that follow, this is an appropriate effective 2D model to capture the 3D slab cavity effects.

To appropriately model fabrication disorder in the effective 2D model, we compared the statistical average and variance of the $L15$'s 3D simulation to varying amounts of structural disorder for the corresponding 2D simulation. Taking the normal definition of our Q factor to be $Q = \frac{\omega}{2\Gamma}$, we can capture the disorder statistics using Γ, as ω is roughly constant with increasing disorder. Defining $\Gamma = \Gamma_0 + \Gamma_{\mathrm{Dis}}$, where Γ_0 is the ideal structure's broadening [full width at half-maximum (FWHM)] and Γ_{Dis} is additional broadening due to structural disorder, we plot $\langle \Gamma_{\mathrm{Dis}}/\Gamma_0 \rangle$ for the 3D data collected in Fig. 3(a) and compare it to 100 instances of 2D simulations with $\sigma_{\mathrm{Dis}} = [0.0025, 0.005, 0.01, 0.02]$ (400 simulations total),

as shown in Fig. 4(d). In our 2D simulations, intrinsic disorder is seen to be best modeled (namely, more similar to 3D) by $\sigma_{\mathrm{Dis}} = 0.01a$.

III. EFFECTIVE TWO-LEVEL ATOM MODEL AND POLARIZATION PLUG-IN EQUATIONS

Here we describe a simple effective gain model for typical experimental QDs [72]. We assume QDs that can be described as effective TLAs, where the physics of higher-order energy levels is effectively ignored (or adiabatically eliminated), and we use an incoherent pump term P to create a positive population inversion and thus gain [73]. While one could implement an optically driven multilevel system [48], in reality the level structure of the QDs is quite rich and vary from dot to dot, so it would not be very meaningful; in addition, as long as the relaxation rates from the higher-lying levels are sufficiently fast, an effective two-level model is expected to be accurate and sufficient for our current study.

To derive the OBEs, we use a master equation to solve for the density matrix of each TLA, and treat the electromagnetic field classically. Starting with the system Hamiltonian of a TLA, with a dipole moment **d** defined by a ground state $|0\rangle$, and excited state $|1\rangle$, with energy difference ω_0, and interacting with an electromagnetic field **E**, we have the system Hamiltonian

$$\mathcal{H} = \frac{\hbar \omega_0}{2}\sigma_z - \hbar\Omega(t)(\sigma^+ + \sigma^-), \tag{5}$$

where the Rabi frequency $\Omega(t) = \frac{\mathbf{d}(t)\cdot\mathbf{E}(t)}{\hbar}$ describes the field interaction with the dipole moment, σ_z is the $z-$ component Pauli matrix, and σ^+ and σ^- are the raising and lowering operators of our TLA, respectively. We stress that the electric field $\mathbf{E}(t)$ is solved self-consistently by FDTD (including the dipole field), while **d** and ω_0 are set by the material plug-in equations, which solve the OBEs derived from the master equation of this Hamiltonian. One can think of this Rabi field as the local or self-consistent Rabi field. Since our QDs of interest are modeled at room temperature, the dominant source of damping is due to nonradiative processes, in particular pure dephasing. The dissipative nature of our QDs environment is included phenomenologically using Lindblad superoperators $\mathcal{L}$, defined as $\mathcal{L}(\mathcal{O})\rho = \mathcal{O}\rho\mathcal{O}^\dagger - \frac{1}{2}(\mathcal{O}^\dagger\mathcal{O}\rho + \rho\mathcal{O}^\dagger\mathcal{O})$. Traditionally, when a TLA interacts with degrees of freedom such as photons, phonons, other collective modes, molecular vibrations, rotations, and translations, it experiences a broadening of its absorption linewidth directly proportional to the total dephasing rate [74]. This broadening has two main contributions in QDs: an inherent relaxation rate Γ_R determined by the TLA's environment (e.g., for maximum coupling $\Gamma_R \propto Q/V_{\mathrm{eff}}$) captured by the FDTD method at all positions, and a pure dephasing rate γ' which is related to the temperature, and to coupling to lattice vibrations in the solid (phonons), and charge noise. We add pure dephasing phenomenologically to our system Hamiltonian via the Lindblad superoperator $\gamma'\mathcal{L}(\sigma^+\sigma^-)$.

To achieve positive population inversion, we include the Lindblad term $P\mathcal{L}(\sigma^+)$, which is responsible for pumping the excited QD lasing state. We neglect any influence from the pump field on additional dephasing [73] (since our largest P

is around 8 ns^{-1}, while our γ' is 1.5 ps^{-1}). In the usual way, we use the quantum Liouville equation $\dot{\rho} = \frac{-i}{\hbar}[\mathcal{H}, \rho]$ with the Lindblad terms to derive equations of motion for the density matrix. The master equation is now given by

$$\frac{d\rho}{dt} = \frac{-i}{\hbar}[\mathcal{H}, \rho] + P\mathcal{L}(\sigma^+)\rho + \gamma_0\mathcal{L}(\sigma^-)\rho + \gamma'\mathcal{L}(\sigma^+\sigma^-)\rho, \tag{6}$$

where $\gamma_0 \approx 0.1\Gamma_{\text{hom}}$ [75] ($\Gamma_{\text{hom}} \approx 0.4$ ns^{-1} is the decay rate in a homogeneous medium, defined later) is the decay rate associated with out-of-plane decay (i.e., via radiation modes above the slab light line), ρ is a 2×2 matrix (for each QD) with diagonal elements ρ_{11} and ρ_{00} associated with the probabilities of being in the excited and ground states, respectively, and off-diagonal elements $\rho_{01} = \rho_{10}^*$ associated with the system's coherence. We define inversion as $\rho_{11} - \rho_{00} = 2\rho_{11} - 1$ since $\rho_{11} + \rho_{00} = 1$. Solving Eq. (6), we find equations of motion for $\dot{\rho}_{11}$ and $\dot{\rho}_{01}$:

$$\frac{d\rho_{11}}{dt} = -2\Omega\rho_{01}^{\text{Im}} + P(1 - \rho_{11}) - \gamma_0\rho_{11}, \tag{7}$$

$$\frac{d\rho_{01}^{\text{Re}}}{dt} = -\omega_0\rho_{01}^{\text{Im}} - \frac{P + \gamma'}{2}\rho_{01}^{\text{Re}} - \frac{\gamma_0}{2}\rho_{01}^{\text{Re}}, \tag{8}$$

$$\frac{d\rho_{01}^{\text{Im}}}{dt} = \omega_0\rho_{01}^{\text{Re}} - \frac{P + \gamma'}{2}\rho_{01}^{\text{Im}} + \Omega(2\rho_{11} - 1) - \frac{\gamma_0}{2}\rho_{01}^{\text{Im}}, \tag{9}$$

where we have separated ρ_{01} into its real $\text{Re}[\rho_{01}] = \rho_{01}^{\text{Re}}$ and imaginary $\text{Im}[\rho_{01}] = \rho_{01}^{\text{Im}}$ parts, thus leaving three coupled equations with only real parameters (per QD); this is done for numerical convenience. Together, these equations define the optical Bloch equations (OBEs) which describe the quantum nature of an effective TLA interacting with a completely general classical electric field via FDTD. This formalism neglects a small frequency shift from the self-field of the emitter, which arises due to the numerically divergent in-phase contribution at the location of the emitter [76], though this has negligible influence on our findings, especially with eventual random center frequencies for each QD emitter.

In deriving Eqs. (7)–(9), we have not made any approximations other than those defined by the model itself (i.e., only two energy levels). This is unusual compared to standard textbook derivations [77,78], which often invoke a rotating-wave approximation; however, this is done as a result of assuming some form for the electric field, whereas we have not assumed any information regarding our quickly varying electric field. Instead, we leave our OBEs quite general, such that the FDTD algorithm captures the light-matter physics experienced by our TLA in a self-consistent way, including radiative decay and dipole-dipole interactions between different QDs. To include the OBE in the FDTD simulations, we use Lumerical's user-defined-material plug-in tool [79], which allows for the creation of customized material responses, written in C++. The plug-in code is called at each time step n, and is used to update the electric field E^n by the polarization density P^n output by the plug-in script. In general, this is written as $U^n E^n + \frac{P^n}{\epsilon_0} = V^n$, where U^n and V^n are inputs provided by Lumerical's software, and E^n is updated along the x, y, and z axes.

To determine the polarization density **P** output by our OBEs, we use $\mathbf{p} = e\mathbf{r}(\rho_{01} + \rho_{01}^*) = 2e\mathbf{r}\,\text{Re}[\rho_{01}]$, such that the polarization density $\mathbf{P} = N\mathbf{p}$ is given by

$$\mathbf{P} = 2\mathbf{d}N\,\text{Re}[\rho_{01}], \tag{10}$$

where $e\mathbf{r} = \mathbf{d}$ is the dipole moment associated with our atom, which assumes our dipole moment is equally strong in all directions, while N is the relevant density of the QD being polarized, defined by

$$N = V_{\text{QD}}^{-1} = \delta(z - z')/(\Delta x \Delta y), \tag{11}$$

where V_{QD}^{-1} is the inverse QD volume (i.e., V_{QD} is the same for each QD, and is defined by the Yee cell volume, or area in this 2D case), and Δx, Δy are the Yee cell dimensions of the FDTD simulation. We note that the assumption to have an equally strong dipole moment in all directions is not representative of natural QD ensembles, and future works could include statistical variations of the dipole moments direction. However, since the optical modes are strongly polarized in a particular direction, we do not expect that it would make much difference to our simulations below. Finally, to implement the OBEs numerically, we use the fourth-order Runge-Kutta method, thus storing only the previous time-step values ρ_{11}^n, $\rho_{01}^{\text{Im},n}$, and $\rho_{01}^{\text{Re},n}$, when updating ρ_{11}^{n+1}, $\rho_{01}^{\text{Im},n+1}$, and $\rho_{01}^{\text{Re},n+1}$, and P^n using Eq. (10).

IV. DIPOLE MOMENT MODEL AND RECOVERING THE CORRECT RADIATIVE DECAY FROM A POINT DIPOLE

In the dipole approximation, where we assume that interacting electromagnetic fields have negligible variation over each quantum emitter, we define the oscillator strength $\mathcal{F}$ of the InAs QD, as $\mathcal{F}(\omega) = \Gamma_{\text{rad,hom}}(\omega)/\Gamma_{\text{HO}}(\omega)$ [80], where $\Gamma_{\text{rad,hom}}(\omega)$ is the homogeneous medium's radiative decay rate, which includes information about the excitonic degrees of freedom, and $\Gamma_{\text{HO}}(\omega)$ is the radiative decay rate of a classical harmonic oscillator of elementary charge. This approximation is valid because of the typical small size of the QDs, ~ 15 nm in diameter (and a few nm in height) [72]. Following Ref. [80], $\mathcal{F}(\omega)$ is proportional to independent electron and hole envelope function $F_e(\mathbf{r}_0, \mathbf{r})$, and $F_h(\mathbf{r}_0, \mathbf{r})$, respectively, in the strong confinement regime, given by $\mathcal{F}(\omega) = \frac{E_p}{\hbar\omega}|\int d\mathbf{r} F_e(\mathbf{r}_0, \mathbf{r})F_h(\mathbf{r}_0, \mathbf{r})|^2$, where E_p is the Kane energy of the QD material. The wave-function overlap $I_{\text{WF}} = |\int d\mathbf{r} F_e(\mathbf{r}_0)\mathbf{r}F_h(\mathbf{r}_0, \mathbf{r})|^2$ is a relatively constant function with respect to QD size, and is mainly dependent on the emission energy of the QD [81]. A QD emitting at 190 THz (0.79 eV), which has an electron-hole overlap $I_{\text{WF}} > 0.8$ [81]. In addition, the Kane energy of bulk InAs to be 21.11 eV [82]. Thus, we assume QDs with an oscillator strength of roughly 17.2 when assuming a wave-function overlap of 80%.
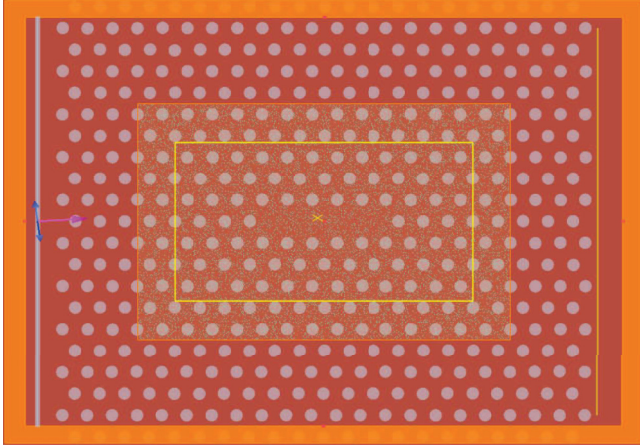
The dipole strength d of our modeled QDs can be calculated directly by the oscillator strength, given by [83]

$$d^2 = \frac{e^2\hbar}{2m\omega}\mathcal{F}, \tag{12}$$

where e is the elementary charge and m is the free-electron mass. Using our oscillator strength $\mathcal{F} = 17.2$, we calculate a dipole moment of 43.88 D (or 0.91 e-nm).
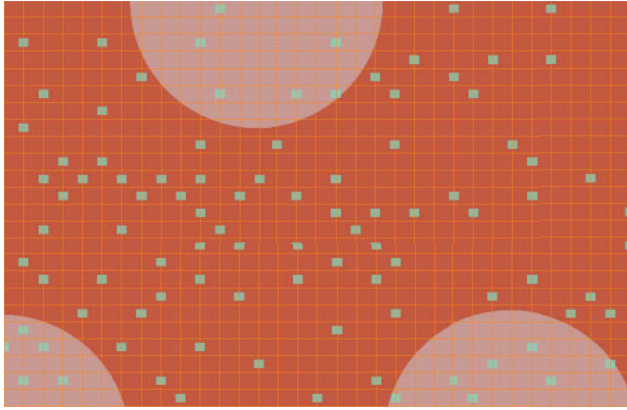
(a)   Zoom in of example QD dipoles at various Yee cells

(b)   Example simulation set up with many QDs in an $L5$

FIG. 5. (a) Quantum-dot dipoles located at E_y along the Yee cell, randomly positioned with no nearest neighbors, with a density of 540 μm^{-2}. The grid dimensions are $dx = 16.8462$ nm and $dy = 14.5892$ nm, while the QD size is made smaller than this to emphasize its location at only a single grid point; however, its size is effectively $dx\,dy$. (b) Quantum-dot gain setup: the orange border is PML boundary conditions, the gray bar on the left is the initial source pulse, which stimulates the optically pumped QD gain region in the center, the yellow rectangle denotes the index and DFT monitors, the yellow cross is a time monitor, and the orange line on the right is a power line monitor that captures the average power out of the cavity, over the last 10 ps. The total number of QDs in this particular simulation is 14 029 (for reference, $L15$ simulations have $\approx$24 000 QDs).

V. QUANTUM-DOT MODELING IN FDTD AND SIMULATION SETUP

To model QDs in FDTD, the TLA plug-in is implemented at a single Yee cell dipole with an area (in 2D) equal to the Yee cell. We choose to implement QDs at E_y field points, seen in Fig. 5(a), as our cavity modes primarily exist in this direction. To better model the QD dimensions, we reduce the mesh steps Δx, Δy to 16.85 and 14.59 nm, respectively, which is asymmetric to maintain uniform meshing across all etched holes (in a triangular lattice). The QDs are then added to our gain region randomly, with an area density $\mathcal{N}_{QD} = 540$ μm^{-2}. The only restriction placed on the QD locations is that no two QDs may be side by side. Each QD field location is given a

background index that matches the substrate material, which is a good approximation since the QD material has an index very near the slab structure. To ensure that no QD is created within the etched holes of the PC, a mesh order is assigned to the QDs to be the second last material added to the system, with etching as the final material, added over-top of all previous indices.

An example simulation setup is shown in Fig. 5(b), which has the following simulation features: a time monitor at its center, an index, and a DFT monitor around the cavity in yellow (inner rectangle) to capture the electric field profiles, a gain region made as small as possible (e.g., the smallest region with the same steady-state output as larger gain regions) to save meshing memory overhead, an incident plane-wave pulse on the left, a power line monitor on the right, and PML boundary conditions all around. The plane wave is angled slightly to excite both E_x and E_y field components, and the power line monitor only captures the last 10 ps of power emitted by the cavity. This is consistent across all cavity lengths simulated, while the time each cavity simulation is run for is determined by how long it takes to reach steady-state lasing.

Since real QD materials have a large fluctuation in the QD emission frequencies, each QD has its energy spacing ω_0 randomly drawn from a normal distribution to better represent slight variations in the QD size that occurs in practice. Thus, nonuniform emission lines lead to inhomogeneous broadening, which can be modeled with parameters obtained from experimental data. At room temperature, InAs QDs are dominated by pure dephasing γ', typically around 1.5 THz (or 6 meV) [33], and the overall inhomogeneously broadened spectra are roughly 10 THz (or 40 meV), as shown by the QD ensemble electroluminescence in Ref. [72]. Thus, we assign each QD a resonant frequency that is selected randomly from a Gaussian distribution modeled after experimental photoluminescence spectra. This model is shown in Fig. 6(a), where the Gaussian distributions variance is 6.6 THz, with mean ω_0. In this way, both QD position and resonant frequency are stochastically modeled.

To further connect our 2D simulations to the 3D dipole interactions, we first model radiative decay using Fermi's golden rule in 3D, which is is well known [84]:

$$\Gamma_a(\mathbf{r}_a) = \frac{2}{\hbar\epsilon_0}\{\mathbf{d}_a \cdot \mathrm{Im}[\mathbf{G}(\mathbf{r}_a,\mathbf{r}_a;\omega)] \cdot \mathbf{d}_a\}, \qquad (13)$$

where $\mathbf{G}$ is then projected in the dominant field direction (in our PC cavities, that is the y direction), at the location of the dipole emitter. This definition of radiative decay assumes we are in 3D space, and our GF has units of inverse volume (m^{-3}), while the dipole moment has units Coulomb meter (Cm), and the overall decay rate has units of inverse seconds (1/s). Assuming radiative decay is calculated with the same formula in 2D, it is then required to introduce an effective length l_z as our GF loses a spatial dimension from 2D to 3D. That is, we define

$$\Gamma_{2D,\mathrm{eff}} = \Gamma_{3D}, \qquad (14)$$

where $\Gamma_{2D,\mathrm{eff}}$ is the radiative decay rate obtained in the 2D simulations. To achieve this, we use the radiative decay rates of free space such that $\Gamma_{2D,\mathrm{free\ space}}/l_z = \Gamma_{3D,\mathrm{free\ space}}$, which

(a) Spectral profiles for different QD numbers

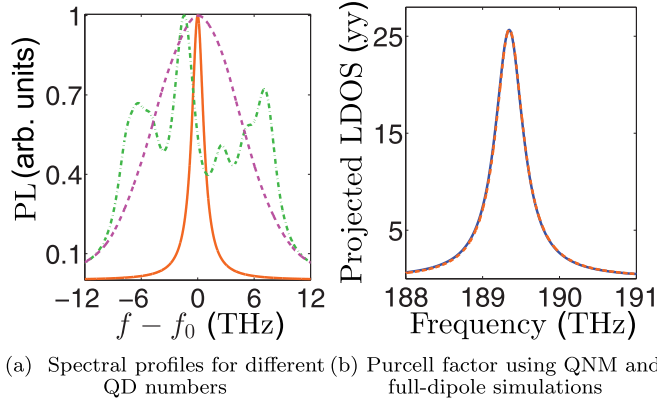(b) Purcell factor using QNM and full-dipole simulations

FIG. 6. (a) Modeled QD ensemble (dashed and dotted-dashed lines) for 10 (green chain) and 10 000 (magenta dashed line) QDs, for typical room-temperature inhomogeneous broadening. The individual QD line shape is given by the orange (light) line, with $\gamma' = 1.5$ THz. The y-shows a normalized photoluminescence (PL) for individual (solid line) and ensembled (dashed or dotted-dashed lines) QDs. The number of QDs in each simulation is on the order of 10 000. (b) Fundamental mode comparison between full-dipole expansion (blue line) and QNM theory (orange dashed line) for low-Q cavity, with a reduced PC membrane. The projected LDOS has been normalized to represent PF.

defines an effective length l_z as

$$l_z = \frac{\Gamma_{\text{2D,free space}}}{\Gamma_{\text{3D,free space}}} = \frac{\mathbf{G}_{\text{2D,free space}}}{\mathbf{G}_{\text{3D,free space}}}. \tag{15}$$

The free-space Green function in 2D is derived as $\text{Im}\{\mathbf{G}_{\text{2D}}^{\text{hom}}\} = \frac{1}{8}\frac{\omega^2}{c^2}$ (for TE modes), while in 3D we have $\text{Im}\{\mathbf{G}_{\text{3D}}^{\text{hom}}\} = \frac{n}{6\pi}\frac{\omega^3}{c^3}$ [85]. Using these definitions in Eq. (15), then

$$l_z = \frac{3\pi}{4n}\frac{c}{\omega}, \tag{16}$$

and the effective radiative decay rate in our simulations is

$$\Gamma_{\text{2D,eff}}(\mathbf{r}) = \frac{8n\omega}{3\pi\hbar\epsilon_0 c}\{\mathbf{d}\cdot\text{Im}[\mathbf{G}_{\text{2D}}(\mathbf{r},\mathbf{r};\omega)]\cdot\mathbf{d}\}. \tag{17}$$

To verify that this model indeed obtains the correct radiative decay from a dipole, we scale our plug-in density N_{eff} by l_z in Eq. (16), such that $N_{\text{eff}}^{-1} = \Delta x \Delta y l_z$, arriving at $N_{\text{eff}} = 1.743 \times 10^4 \, \mu\text{m}^{-3}$ for $\omega = 190$ THz. We then model our plug-in material at a single Yee cell at the center of an $L5$ cavity, and employ an initially excited state to measure the natural decay of the TLA, and turn off phenomenological decays γ', γ_0, and the incoherent pump P. Thus, there are no phenomenological terms in the OBE at all, either radiative or nonradiative. We set the dipole moment magnitude to 43.88 D to mirror the values that will be used in the ensemble simulations below. To initially ensure we are not near the strong-coupling regime, we first set up our 2D cavity to have a low-Q factor, by shortening the PC membrane on either side of the cavity edge. We give the TLA an initial polarization to simulate a dynamical decay from a radiation reaction (which is known to give the same decay as from vacuum fluctuations). From this simulation, we find very good agreement between theory and simulation, where the GF of our cavity is calculated with Eq. (1), which is shown to
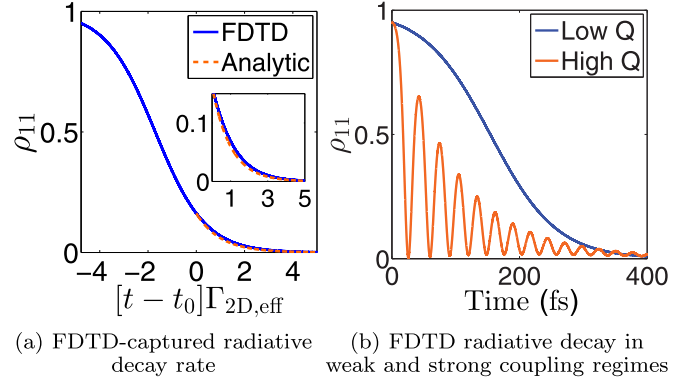

(a) FDTD-captured radiative decay rate

(b) FDTD radiative decay in weak and strong coupling regimes

FIG. 7. (a) Population ρ_{11} dynamics within an $L5$ low Q-factor (≈ 400) cavity, solved by MBE without any decay terms, so all phenomenological decay parameters are set to zero and the radiative decay is captured self-consistently through the local electric field used in the OBE solver. The OBEs are given initial conditions $\rho_{11}(t = 0) = 0.95$, $\rho_{01}^{\text{Im}}(t = 0) = 0$, and $\rho_{01}^{\text{Re}}(t = 0) = \sqrt{1 - 0.95^2}/2$, such that the Bloch vector magnitude is set to unity (e.g., $\sigma_1 = 2\rho_{11} - 1$, $\sigma_2 = 2\rho_{01}^{\text{Re}}$, and $\sigma_3 = 2\rho_{01}^{\text{Im}}$ are the usual Bloch vector components with magnitude $\sigma_1^2 + \sigma_2^2 + \sigma_3^2$). The analytic solution is determined by $\Gamma_{\text{2D,eff}}$, calculated by the QNM GF seen in Fig. 6(b). (b) Comparison of high- and low-Q cavities for the 2D $L5$ cavity structure, which were 47 000 and 430, respectively. All other parameters are the same as in (a).

agree with numerically exact (i.e., full-dipole) simulations in Fig. 6(b). Importantly, this accuracy will be maintained at any spatial position within our simulation array of multiple dipoles. We also stress that the FDTD also captures QD-QD radiative interactions [86], which in a master-equation approach would be computed from terms like

$$\Gamma_{ab}(\mathbf{r}_a \to \mathbf{r}_b) = \frac{2}{\hbar\epsilon_0}\{\mathbf{d}_a \cdot \text{Im}[\mathbf{G}(\mathbf{r}_a,\mathbf{r}_b;\omega)] \cdot \mathbf{d}_b\}, \tag{18}$$

and a corresponding Lamb shift [87]. Clearly including such terms in an ensemble of different QDs, in the many thousands (and even in the tens), would be intractable in a standard master equation approach. Dipole-dipole coupling has recently been shown to have a strong impact on the subradiance and superradiance on steady-state QD laser systems [88], thus increasing the importance to model it correctly in such systems.

To fit our simulations for the single dipole Γ_{Num} with $\Gamma_{\text{2D,eff}}$, we match decay lifetimes as seen in Fig. 7(a). Note, the initial decay of ρ_{11} is nonexponential because its inversion level is positive, thus the electric field emitted initially grows in magnitude as a consequence of the initial condition. Once our QD becomes an absorber ($\rho_{11} < 0.5$), we start to recover the expected exponential decay shape of radiative decay, which eventually becomes fully exponential at t_0. Finally, in Fig. 7(b), we compare our low-Q cavity to the usual high-Q simulation, and find the semiclassical analog of vacuum Rabi oscillations, namely, we get periodic cycles of the population at a rate given by $2g = \Omega_{\text{Rabi}}$ [83,89], where g is the QD-cavity coupling rate (which scales with d^2/V_{eff}) and Ω_{Rabi} is the width of the frequency splitting in frequency space.

VI. MAIN SIMULATION RESULTS OF GAIN THRESHOLD FOR A QD ENSEMBLE IN PC CAVITIES OF DIFFERENT LENGTH

A. QD ensemble

Using the QD ensemble defined above, we are now ready to simulate gain in the 2D PC cavities, in a self-consistent way. The simulation domain is described in Sec. V [see Fig. 5(b)]. The only parameter left undefined is the inhomogeneous ensemble's peak frequency ω_0. As the homogeneous PC has a band gap between 185–215 THz, the peak frequency should be somewhere within this range. We define two different center ω_0 values to study two different gain models: $\omega_1 = 187$ THz (gain model A) and $\omega_2 = 197$ THz (gain model B), which results in two different gain spectra from the QD ensemble, shown in Fig. 8(b). These two values were chosen to represent two different gain regimes: mainly single-mode lasing over all cavity lengths (which was seen and reported in Ref. [13]) performed by ω_1 (model A), as the mode nearest resonance is always the first fundamental mode; and a peak frequency determined by the electroluminescence for the QD used in Ref. [13], performed by ω_2 (model B). Simulations with ω_1 and ω_2 are carried out with all other parameters equal for consistency. Figure 8(a) compares the peak frequency of the first five fundamental modes as a function of cavity length to the resonant frequency of the two QD ensembles from Fig. 8(b).

FIG. 9. Lasing dynamics (field in arbitrary units) of an $L5$ cavity given a QD ensemble with ω_1 (gain model A), as measured at the center of the cavity ($x = y = 0$). The pump rate of 0.1 ns^{-1} does not lase and only decays, while a pump rate 1 ns^{-1} is into the lasing regime, as it increases in amplitude, followed by decay as it finds its equilibrium, and a pump rate 8 ns^{-1} is clearly well into the lasing regime.

(a) Cavity frequencies versus length
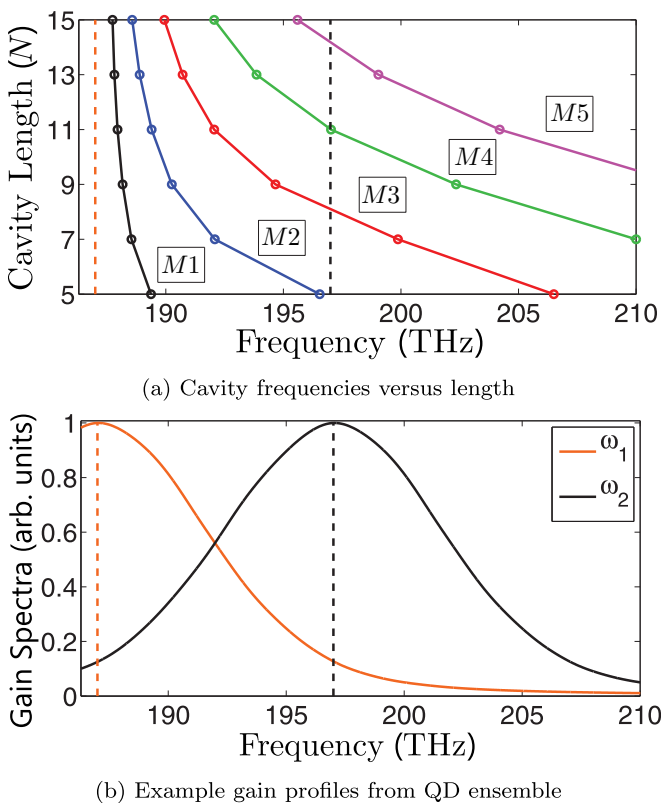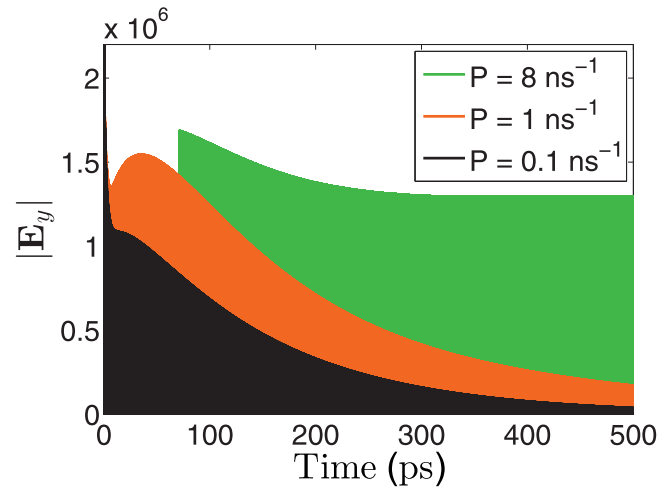

(b) Example gain profiles from QD ensemble

FIG. 8. (a) Dependence of the cavity mode peak frequencies, for each cavity length, to the resonant peak QD ensemble gain (or PL) spectra. (b) Visualization of the normalized imhomogeneously broadened gain spectra of the QD ensemble for ω_1 (gain model A) and ω_2 (gain model B) taken from Fig. 6(a).

Although the pumped QDs do not need any additional optical source to achieve lasing, we find SS can be reached much more quickly when an external (linear) plane-wave source [seen in Fig. 5(b)] initially excites the cavity. The downside of this approach is that some amount of power will always be captured by the power monitor, which is discussed in the next subsection. However, the lasing threshold is determined by the slope taken from simulations that are clearly lasing. The dynamics of each simulation is obviously different depending on if the cavity is below, near, or above threshold, as is shown in Fig. 9, where a pump rate of 0.1 ns^{-1} only decays, while 1 ns^{-1} increases, followed by decay as it finds its equilibrium, and 8 ns^{-1} is well into the lasing regime, finding equilibrium quickly.

The pump threshold P_{th} is defined by the usual method of extending the linear region of a "light-in–light-out" (LL) curve down to the x axis, as shown in Fig. 10 for ω_1 (model A) [the results for ω_2 (model B) are qualitatively similar]. Comparing the low-resolution transmission spectra, measured along a line at the end of the PC membrane as depicted in Fig. 5(b), in Sec. V, for the $L7$ and $L15$ cavities of these two different QD ensembles, we see that ω_1 is predominantly a single-mode laser [Figs. 11(a) and 11(b)], while ω_2 is more clearly multimode [Figs. 11(c) and 11(d)]. A major advantage of our model is that is is able to capture all optical modes that appear in the light-matter coupling.

B. Role of QD ensemble characteristics and a nonuniform radiative decay rate

The pump thresholds for each cavity length were first performed with several QD instances to check for significant fluctuations in any of the trend lines. An example of this can be seen in Fig. 12(a), where a reasonable variation was seen between $L13$ and $L15$ pump thresholds. All other
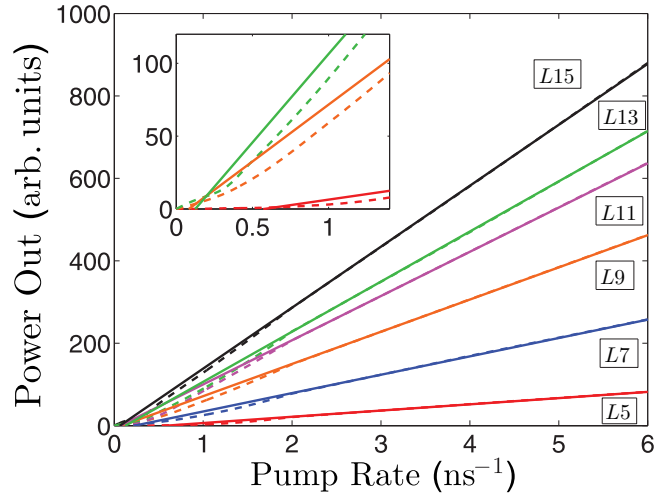
FIG. 10. Example lasing curve, or LL graphs of the ω_1 QD ensemble, where the dashed lines represent simulated data, and solid lines are the linear fit used to extract pump threshold. The inset is a closeup of the $L5$, $L9$, and $L13$ curves.

pump thresholds represent a single instance, and any error or uncertainty in the computations of single instance gain threshold is determined by the maximum and minimum fitted slopes, and uncertainty in the y intercept. There is some uncertainty in the y intercept due to artificial power measurements at low pump strengths, which is caused by the initial source amplitude continuing to leak into the power monitor at the end of the simulation, due to the high-Q factors of the cavities. As such, there exists a positive y intercept for the measured power emitted by the cavity, when the pump rate is set to zero. This can be seen in Fig. 13, which is an $L9$
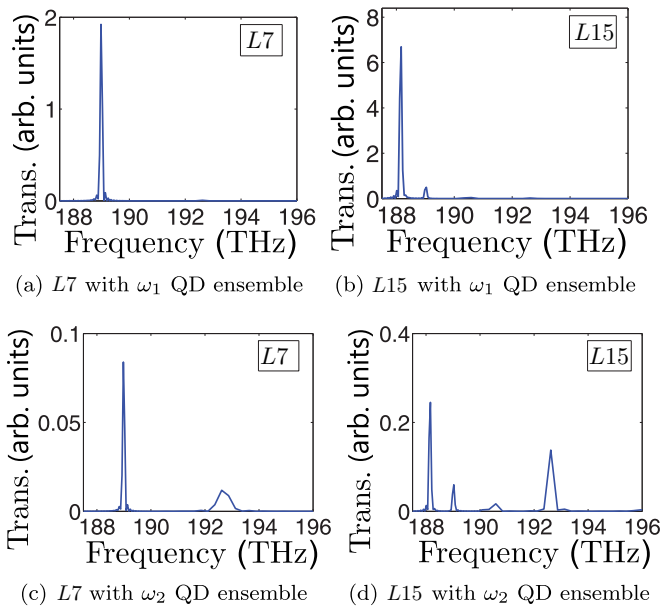

(a) $L7$ with ω_1 QD ensemble

(b) $L15$ with ω_1 QD ensemble

(c) $L7$ with ω_2 QD ensemble

(d) $L15$ with ω_2 QD ensemble

FIG. 11. (a), (b) Example transmission measured at the output power DFT monitor for lasing $L7$ (a) and $L15$ (b) cavities ($P = 8$ ns^{-1}) the ω_1 QD ensemble. (c), (d) Example transmission measured with the ω_2 QD ensemble.

(a) Average versus example instances of gain threshold

(b) Threshold behaviour for two different QD gain profiles

(c) Ensemble versus a sheet density (spatially uniform gain)

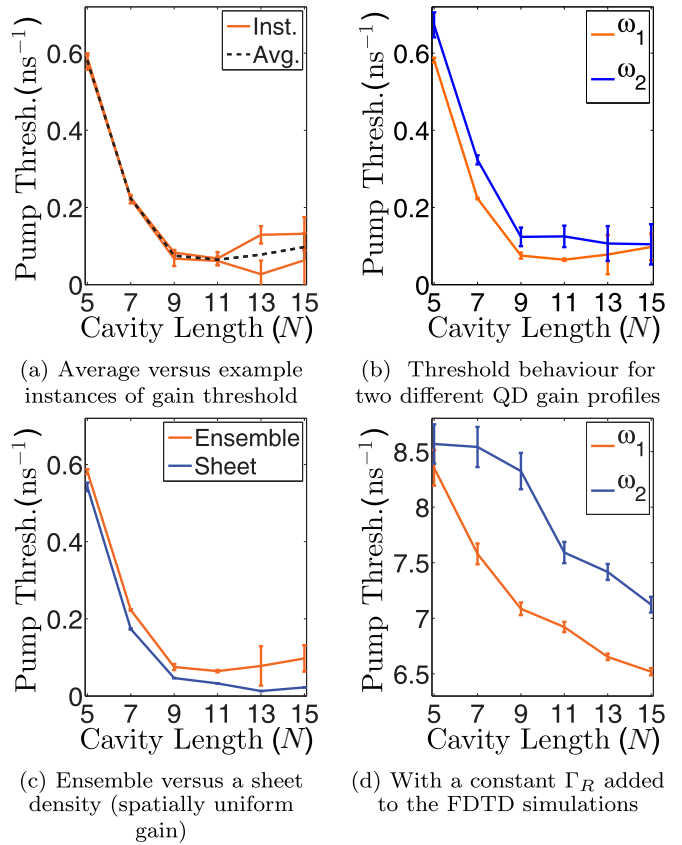(d) With a constant Γ_R added to the FDTD simulations

FIG. 12. Pump gain thresholds extracted from LL curves for various setups. Error bars on individual instances are determined by the maximum and minimum fitted slopes, and any uncertainty in the y intercept due to artificial power measurements at low pump strengths caused by early terminations of the simulations (as demonstrated in Fig. 13). (a) The average (dotted black line) of only two QD instances (orange lines) of ω_1. (b) A comparison of ω_1 (gain model A) and ω_2 (gain model B) simulations. (c) A comparison of the sheet simulation to the average QD simulations. (d) Thresholds given by simulations with a phenomenological radiative decay rate Γ_R, set to 0.05 THz, for all QDs, for both ω_1 and ω_2 gain models.

simulation from one of the two QD instances for ω_1 plotted in Fig. 12(a), with an originally negative pump threshold due to this artifact. To remove the artifact, we fit the low pump data to a polynomial curve, and extract a fitted y intercept, which we use to shift the original data to have a y intercept of zero. The error of this fit is then added in quadrature to the slopes error. The average threshold trend is shown in Fig. 12(a) for ω_1 simulations and compared to ω_2 in Fig. 12(b).

Next, focusing on the dominant single-mode lasing regime, we compare the QD ensemble with simulations that exclude the ensemble statistics by replacing the active gain region with a single plug-in sheet that uniformly excites the various cavity modes. This "sheet" simulation has a pure dephasing value equal to the inhomogeneously broadened ensemble of 10 THz, a peak frequency of ω_1, and a dipole moment $d = 5.84$ D (which was found to model the average dipole moment of the ensemble), and $N_{\text{eff}} = 1.045 \times 10^5$ μm^{-3}, which was used as a fitting parameter to get the $L5$ pump threshold behavior similar to those with the QD ensemble value. The resulting
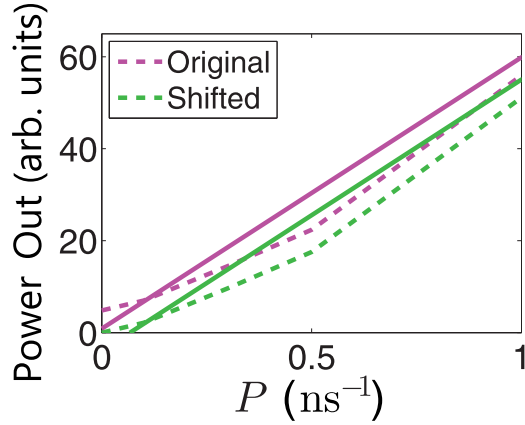
FIG. 13. Example of y-intercept artifact in our simulations, which is due to the large-Q factor of our cavities that inherently emit trapped radiation beyond the end of the finite-time simulation.

pump threshold is shown in Fig. 12(c), compared to the average QD ensemble, which shows a lesser plateauing effect, and increasing pump threshold for increasing cavity lengths. We observe that the spatial-dependent coupling of radiative decay and gain coupling certainly has a qualitatively important role on the gain threshold characteristics and such behavior would be extremely difficult to capture in a simplified rate-equation analysis. Moreover, our findings, though somewhat surprising, are indeed consistent with the unusual experimental trends found by Xue *et al.* [13], who attributed the threshold behavior to structural disorder.

To better understand the effects of the FDTD computed radiative decay rates as a function of cavity length (and the general nonuniform sampling of a radiative decay rate), in Fig. 12(d) we have introduced an additional phenomenological radiative decay rate into the OBEs, Γ_R using the Lindblad superoperator $\Gamma_R \mathcal{L}(\sigma^-)\rho$, and set $\Gamma_R = 0.05$ THz (50 ps^{-1}), which is roughly 100 times smaller than the maximally coupled QD decay rate, averaged over all cavity lengths. However, typically, this will now be the dominant radiative decay process in the simulation. By reducing the natural cavity length dependence of the radiative decay captured by the FDTD method, we see the effects of cavity resonance coupling more clearly, which is reflected in the pump threshold trend in Fig. 12(d). That is, the trend of model A's pump threshold now consistently decreases, as the on-resonant peak cavity PF increases and the resonant mode $M1$ does not significantly change its frequency position with respect to ω_1. On the other hand, the trend of ω_2 is clearly impacted by how close any particular mode is to resonance (e.g., highlighted by a dip in the threshold between $L9$ and $L11$, as resonance conditions are met, and a missing dip between $L5$ and $L7$, as resonance conditions are removed). In either case, this fixed Γ_R, even though much smaller than γ', clearly has a qualitative influence on the gain threshold characteristics and thus the nonuniform sampling of such an effect is important.

C. Discussion and connection to simplified laser rate equations

Although it is difficult to identify the main process responsible for explaining the qualitative difference in gain

threshold behavior shown in Fig. 12(c) (with a plateau) and Fig. 12(d) (monotonous reduction), we speculate as follows: If Γ_R and the gain for all QD emitters is forced to be identical (i.e., not captured self-consistently), all emitters then contribute to the pump rate and the gain. However, in the full calculations only a fraction of the emitters actually contribute to the gain since such values are still calculated from the actual field from the self-consistent FDTD algorithm. Thus, only the fraction of emitters contributing to the gain will be affected when the cavity loss rate is changed with different cavity lengths. For example, if the cavity length is increased and the Q factor decreases, less gain is needed for lasing and the pump threshold will decrease, but there is still a large background pump rate due to all the emitters that do not contribute to the gain. Thus, we suggest that if there is a fixed (and dominant) Γ_R, then this relatively large background pump rate may act to mask small absolute changes in the threshold gain [compare absolute scales in Figs. 12(c) and 12(d)]. A possible reason for the plateauing of the gain threshold is that the effective gain seen by the QDs changes substantially depending upon the cavity length. We elaborate on this point in more detail below by connecting to common cavity laser rate equations. In Ref. [13], it was shown that the experimental results could be explained if one assumes a cavity loss rate that increases with the group refractive index. However, this assumption, at least for the passive cavity, is challenged by the simulation results of Fig. 1. Using the simple rate equations, e.g., of Prieto *et al.* [28] for the carrier and photon densities of a QD PC cavity laser system (neglecting nonradiative decay in the carrier density equation), then

$$\frac{dN^e}{dt} = R_p - N^e\Gamma_R - g c_{\mathrm{eff}}\left(N^e - N_0^e\right)N^{\mathrm{ph}}, \quad (19)$$

$$\frac{dN^{\mathrm{ph}}}{dt} = \Gamma_{\mathrm{cf}} g c_{\mathrm{eff}}\left(N^e - N_0^e\right)N^{\mathrm{ph}} + \Gamma_{\mathrm{cf}}\beta N^e\Gamma_R - N^{\mathrm{ph}}\Gamma_c, \quad (20)$$

where $c_{\mathrm{eff}} = c/n_{\mathrm{eff}}$, g is the differential gain coefficient, $\Gamma_c = \omega_c/Q$, and Γ_{cf} is an effective confinement factor. From these equations, they estimate an approximate pumping threshold for lasing:

$$P_{\mathrm{th}} \propto R_p^{\mathrm{th}} \propto N_{\mathrm{th}}^e(1-\beta)\Gamma_R, \quad (21)$$

with the corresponding threshold density

$$\begin{aligned} N_{\mathrm{th}}^e &= N_0^e + \frac{\Gamma_c(N)}{\Gamma_{\mathrm{cf}}(N)c_{\mathrm{eff}}g} \\ &= N_0 + \frac{\omega_c(N)}{Q(N)\Gamma_{\mathrm{cf}}(N)c_{\mathrm{eff}}g}, \end{aligned} \quad (22)$$

suggesting that N_{th}^e goes down as Q goes up (longer cavities), implying that P_{th} should come down for increasing cavity lengths. However, one also has to recognize that the $\Gamma_{\mathrm{cf}}(N)$, with N the cavity length, will involve a complex spectral (and spatial) coupling between the QDs and cavity mode(s). Our simulations point to a clear failure of such simple rate-equation approaches for these complex nanophotonic cavity systems, that is perhaps caused by an overall decrease in the effective gain caused by a spectral sharpening of the cavity modes, in addition to possible disorder-induced scattering effects. To

gain some insight into how the LDOS changes at the QD sites for each cavity, below we show the main cavity mode radiative decay rates.

D. Role of spatially varying radiative decay rates

So far, we have exemplified our self-consistent numerical approach that agrees quite well with experimental gain threshold behavior without any structural disorder (which somewhat contradicts earlier assumptions), yet it is not clear why this happens. In an attempt to understand the changing radiative decay rates (and more generally the LDOS, which will also affect the QD gain) from an analytical perspective, we can easily use the fundamental QNM spatial profiles to compute $\Gamma_a(\mathbf{r}_a)$, using Eq. (18), and statistically sample a wide range of spatial points subjected to the same frequency averaging as described above for the QD ensemble (each one assigned a random center frequency). In Fig. 14, we demonstrate the $M1$ projected radiative decay rates sampled over a wide range of spatial points with random frequencies assigned as before; namely, we use the QNM expansion of the GF, through Eq. (1), using just this normalized cavity mode.

FIG. 15. Total ensemble average of the single QD radiative decay rate for each LN cavity averaged over 50 statistical variations of each instance shown in Fig. 14. In contrast to the peak Purcell factor trends, we clearly see a decrease in the average radiative decay rate for increasing cavity lengths that would be randomly sampled by the QDs.

Instead of an increasing decay rate, we see a decrease of the radiative decay rates for increasing length cavities since the probability of spectrally overlapping with the larger-Q cavity modes decreases. To help quantify this effect, we have repeated these statistical simulations 50 times each and computed the ensemble spatial average per LN cavity and confirm that there is indeed a decrease as shown in Fig. 15. Thus, it seems likely that this decreasing radiation decay rate causes an increase in the threshold gain characteristics, and perhaps will plateau as the average increase falls below γ_0 (associated with out-of-plane decay of the PC slab). While the rates are much smaller than γ' (1.5 ps^{-1}), they still play a key role in determining the overall population decay. This view is further supported by the calculations shown in Fig. 12(d), where a fixed (and dominant) radiative decay rate $\Gamma_R = 0.05$ ps^{-1} ($\ll\gamma'$) increases the threshold currents by at least an order of magnitude [cf. Fig. 12(c)], and completely changes the threshold gain characteristics as a function of cavity length.

VII. CONCLUSIONS

We have developed a self-consistent numerical model to describe an active QD ensemble coupled to PC cavities using Lumerical's plug-in tool within an effective 2D FDTD method to investigate pump threshold as a function of cavity length. Both multimode and (primarily) single-mode lasing was found, depending on the peak frequency of the QD ensemble. Studying the effects of our ensemble on the single-mode lasing, we found a general plateauing (and possible increase) of the pump threshold beyond $L9$, in qualitative agreement with recent experiments. As such, we believe there is strong desire to generalize the common rate equations for these complex cavity systems. From a simple analytical modal theory of the fundamental cavity mode, we have also demonstrated how the overall radiative decay rates (and likely other related effects such as the effective gain) can come down as a function of cavity size, which is caused by a reduction in the spectral overlap of the spectrally sharp cavity modes with respect to the broad emission frequencies of the QD ensemble. In the Appendix, structural disorder is also shown to generally increase the pump threshold for cavities longer than $L7$, again in good agreement with the experimental findings of

(a) L5 radiative decay rates

(b) L7 radiative decay rates

(c) L9 radiative decay rates

(d) L11 radiative decay rates

(e) L13 radiative decay rates
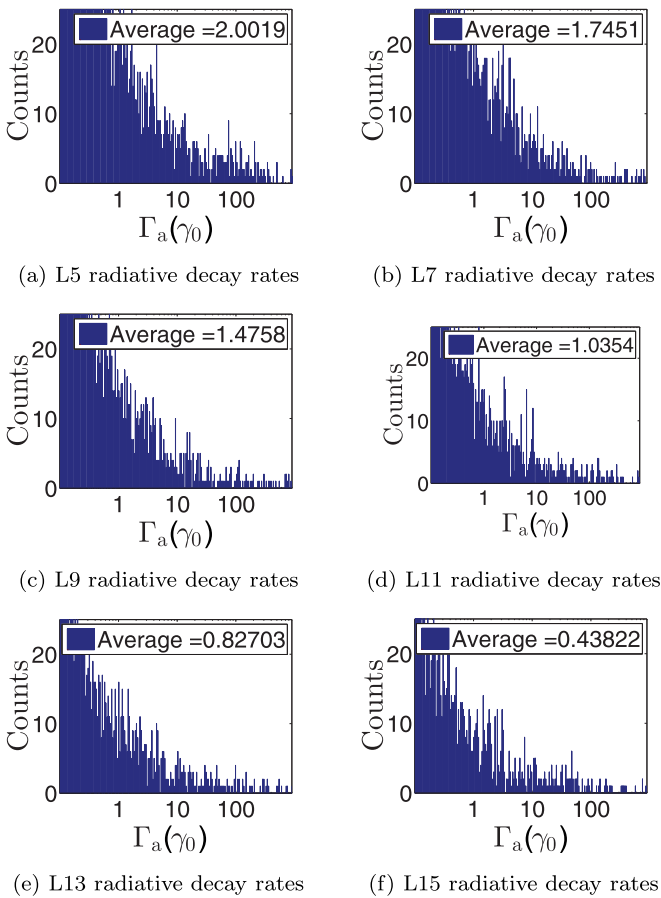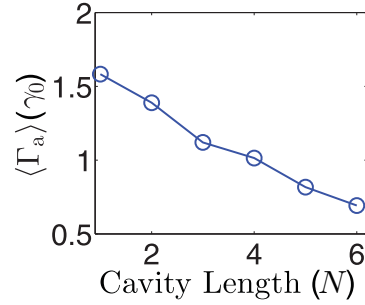
(f) L15 radiative decay rates

FIG. 14. For each cavity length, we show an example instance of the bar-graph statistics from 300 bins of the single-position radiative decay rates overlapping with the fundamental ($M1$) cavity mode, where the center frequencies of the dipole emitters are randomly assigned as before. The total average enhancement rates for each statistical distribution, using all spatial points in the spatial mode active region, is shown in each panel (in units of γ_0).

Ref. [13], though it seems unlikely that disorder alone was responsible for this effect (as our simulations without disorder clearly show). Random localization due to disorder of the lasing cavities modes is also seen, which could merit further investigation, e.g., in the context of slow-light PC waveguides [58,90] and active waveguides [91].

APPENDIX: EXAMPLES OF SINGLE-INSTANCE DISORDERED LATTICES ON THE GAIN THRESHOLD BEHAVIOR

In this Appendix, we briefly assess the impact of single-instance structural disorder on the lasing pump threshold, namely, in the presence of the self-consistent gain dynamics. As mentioned in Sec. II, the intrinsic level of disorder for our effective 2D simulations is given by $\sigma_{\mathrm{Dis}} = 0.01a$ (which mimic the same effect as full 3D slab cavities properties). To understand the effects of additional lattice disorder, we increase this to $\sigma_{\mathrm{Dis}} = 0.04a$. Instances of these two disordered simulations can be seen in Figs. 16(a) and 16(b), where we again use ω_1 as the peak frequency (gain model A). A general increase to the pump threshold, which becomes more prominent beyond $L7$, is clearly seen. These results are indeed consistent with the experimental results from [13], showing that the las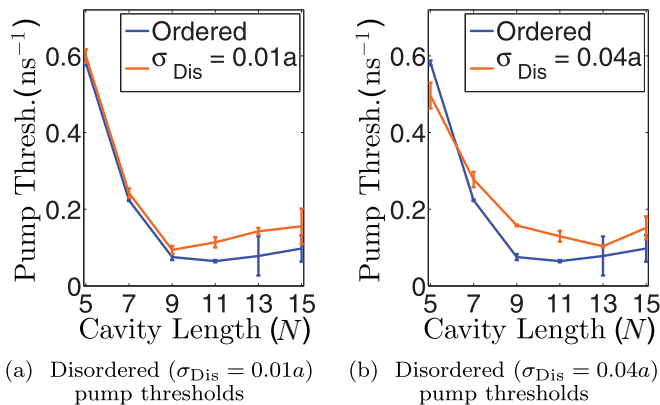er threshold plateaus for increasing cavity length. Our results show that the inhomogeneous nature of the ensemble of quantum dots plays a strong role in this effect, and may even dominate the effects of structural disorder.
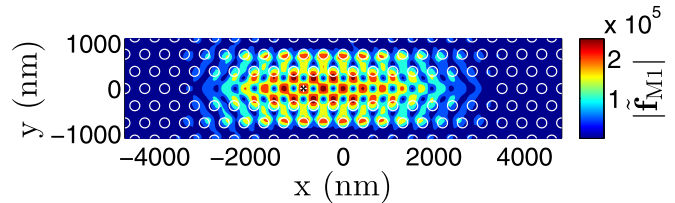
Finally, we also look at the influence of increased disorder (e.g., deliberate disorder) on our lasing mode profiles in the possible regime of Anderson localization, or with strongly localized modes. At $L15$, the $M1$ is the strongest mode
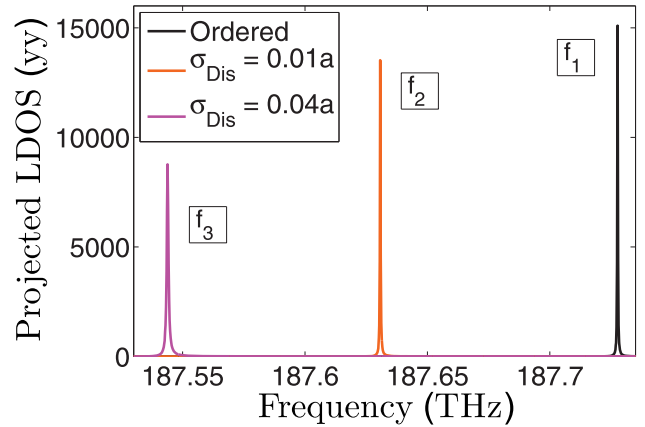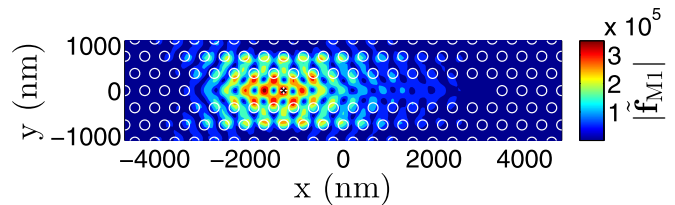

(a) L15 cavity LDOS for ordered, and disordered M1 modes
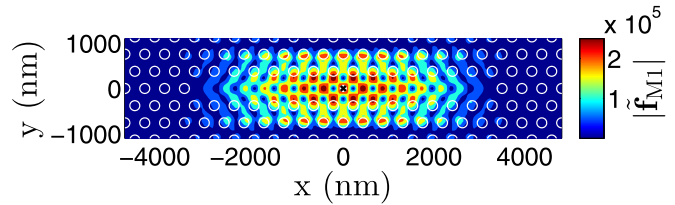
(b) Ordered cavity mode profile, f₁ above

(c) Disordered ($\sigma_{\mathrm{Dis}} = 0.01a$) cavity mode profile, f₂ above

(d) Disordered ($\sigma_{\mathrm{Dis}} = 0.04a$) cavity mode profile, f₃ above

FIG. 17. (a) Projected LDOS along the y direction for the first fundamental lasing mode of the $L15$ cavity, for the sheet active region with peak frequency ω_1, with increasing amounts of disorder. The LDOS is normalized to free space such that our y axis is in units of PF. All lasing modes are measured for simulations with incoherent pump rate $P = 8$ ns^{-1}, where the ordered simulation's response is in black, the intrinsically disordered simulation $\sigma_{\mathrm{Dis}} = 0.01a$ is in orange, and the additional disordered simulation $\sigma_{\mathrm{Dis}} = 0.04a$ is in magenta. (b)–(d) Mode profiles of $M1$ for the ordered (b), intrinsic disordered $\sigma_{\mathrm{Dis}} = 0.01a$ (c), and additional disordered $\sigma_{\mathrm{Dis}} = 0.04a$ (d) simulations.

(a) Disordered ($\sigma_{\mathrm{Dis}} = 0.01a$) pump thresholds

(b) Disordered ($\sigma_{\mathrm{Dis}} = 0.04a$) pump thresholds

FIG. 16. Pump threshold trends for two disordered simulations: intrinsic levels $\sigma_{\mathrm{Dis}} = 0.01a$ (a), and larger than intrinsic disorder $\sigma_{\mathrm{Dis}} = 0.04a$ (b), demonstrating a general increase in the pump threshold predominantly for cavity lengths greater than $L7$.

(highest Q) of all the cavity lengths, and also has the longest mode profile, which makes it the best candidate for localization. Sheet (uniform) gain is used in this analysis to isolate the randomness in the systems to the disorder of the PC. Figures 17(b)–17(d) depict the localization of the fundamental mode as disorder is increased, although the overall PF is still less than the idealized structure as shown in Fig. 17(a). The projected LDOS is measured at the peak antinode location for each mode, which is marked in each mode profile by the small black "x" marker. This localization is random in nature, which potentially limits the applications of such a mode, and although the mode volume is reduced, the Q factor takes an even greater hit. Note with greater disorder comes a larger Q variance, as seen in Fig. 4(d), which does mean it is possible for these localized modes to have reduced mode volume and increased Q factors.

[1] J. L. Jewell, J. P. Harbison, Axel Scherer, Y. H. Lee, and L. T. Florez, Vertical-cavity surface-emitting lasers: design, growth, fabrication, characterization, IEEE J. Quantum Electron. **27**, 1332 (1991).

[2] J. P. Dowling, M. Scalora, M. J. Bloemer, and C. M. Bowden, The Photonic Band Edge Laser: A New Approach to Gain Enhancement, J. Appl. Phys. **75**, 1896 (1994).

[3] S. Droulias, C. Fietz, P. Zhang, T. Koschny, and C. M. Soukoulis, Lasing threshold control in two-dimensional photonic crystals with gain, Opt. Express **22**, 19242 (2014).

[4] M. Meier, A. Mekis, A. Dodabalapur, A. Timko, R. E. Slusher, J. D. Joannopoulos, and O. Nalamasu, Laser action from two-dimensional distributed feedback in photonic crystals, Appl. Phys. Lett. **74**, 7 (1999).

[5] M. Imada, S. Noda, A. Chutinan, T. Tokuda, M. Murata, and G. Sasaki, Coherent two-dimensional lasing action in surface-emitting laser with triangular-lattice photonic crystal structure, Appl. Phys. Lett. **75**, 316 (1999).

[6] S. Riechel, C. Kallinger, U. Lemmer, J. Feldmann, A. Gombert, V. Wittwer, and U. Scherf, A nearly diffraction limited surface emitting conjugated polymer laser utilizing a two-dimensional photonic band structure, Appl. Phys. Lett. **77**, 2310 (2000).

[7] Han-Youl Ryu, Soon-Hong Kwon, Yong-Jae Lee, Yong-Hee Lee, and Jeong-Soo Kim, Very-low-threshold photonic band-edge lasers from free-standing triangular photonic crystal slabs, Appl. Phys. Lett. **80**, 3476 (2002).

[8] Soon-Hong Kwon, Han-Youl Ryu, Guk-Hyun Kim, Yong-Hee Lee, and Sung-Bock Kim, Photonic bandedge lasers in two-dimensional square-lattice photonic crystal slabs, Appl. Phys. Lett. **83**, 3870 (2003).

[9] Xiaohua Wu, Alexey Yamilov, Xiang Liu, Shuyou Li, V. P. Dravid, R. P. H. Chang, and Hui Cao, Ultraviolet photonic crystal laser, Appl. Phys. Lett. **85**, 3657 (2004).

[10] F. Raineri, G. Vecchi, A. M. Yacomotti, C. Seassal, P. Viktorovitch, R. Raj, and A. Levenson, Doubly resonant photonic crystal for efficient laser operation: Pumping and lasing at low group velocity photonic modes, Appl. Phys. Lett. **86**, 011116 (2005).

[11] C. Karnutsch, M. Stroisch, M. Punke, U. Lemmer, J. Wang, and T. Weimann, Laser diode-pumped organic semiconductor lasers utilizing two-dimensional photonic crystal resonators, IEEE Photonics Technol. Lett. **19**, 741 (2007).

[12] D. Luo, X. W. Sun, H. T. Dai, Y. J. Liu, H. Z. Yang, and W. Ji, Two-directional lasing from a dye-doped two-dimensional hexagonal photonic crystal made of holographic polymer-dispersed liquid crystals, Appl. Phys. Lett. **95**, 151115 (2009).

[13] W. Xue, Y. Yu, L. Ottaviano, Y. Chen, E. Semenova, K. Yvind, and J. Mørk, Threshold Characteristics of Slow-Light Photonic Crystal Lasers, Phys. Rev. Lett. **116**, 063901 (2016).

[14] W. Cao, A. Muñoz, P. Palffy-Muhoray, and B. Taheri, Lasing in a three-dimensional photonic crystal of the liquid crystal blue phase ii, Nat. Mater. **1**, 111 (2002).

[15] H.-G. Park, S.-H. Kim, S.-H. Kwon, Y.-G. Ju, J.-K. Yang, J.-H. Baek, S.-B. Kim, and Y.-H. Lee, Electrically driven single-cell photonic crystal laser, Science **305**, 1444 (2004).

[16] H. Noda, T. Tanizaki, T. Gyohten, K. Dosaka, M. Nakajima, K. Mizumoto, K. Yoshida, T. Iwao, T. Nishijima, Y. Okuno et al., The circuits and robust design methodology of the massively parallel processor based on the matrix architecture, in *2006 Symposium on VLSI Circuits, 2006. Digest of Technical Papers* (IEEE, Piscataway, NJ, 2006), pp. 210–211.

[17] K. A. Atlasov, M. Calic, K. F. Karlsson, P. Gallo, A. Rudra, B. Dwir, and E. Kapon, Photonic-crystal microcavity laser with site-controlled quantum-wire active medium, Opt. Express **17**, 18178 (2009).

[18] S. Matsuo, A. Shinya, T. Kakitsuka, K. Nozaki, T. Segawa, T. Sato, Y. Kawaguchi, and M. Notomi, High-speed ultracompact buried heterostructure photonic-crystal laser with 13 fj of energy consumed per bit transmitted, Nat. Photonics **4**, 648 (2010).

[19] M. Nomura, N. Kumagai, S. Iwamoto, Y. Ota, and Y. Arakawa, Laser oscillation in a strongly coupled single-quantum-dot–nanocavity system, Nat. Phys. **6**, 279 (2010).

[20] J. Mørk, Y. Chen, and M. Heuck, Photonic Crystal Fano Laser: Terahertz Modulation and Ultrashort Pulse Generation, Phys. Rev. Lett. **113**, 163901 (2014).

[21] Y. Yu, W. Xue, E. Semenova, K. Yvind, and J. Mørk, Demonstration of a self-pulsing photonic crystal fano laser, Nat. Photonics **11**, 81 (2017).

[22] P. T. Kristensen and S. Hughes, Modes and mode volumes of leaky optical cavities and plasmonic nanoresonators, ACS Photonics **1**, 2 (2013).

[23] E. S. C. Ching, P. T. Leung, A. Maassen van den Brink, W. M. Suen, S. S. Tong, and K. Young, Quasinormal-mode expansion for waves in open systems, Rev. Mod. Phys. **70**, 1545 (1998).

[24] G. Fujii, T. Matsumoto, T. Takahashi, and T. Ueta, Study on transition from photonic-crystal laser to random laser, Opt. Express **20**, 7300 (2012).

[25] S. Shi and D. W. Prather, Lasing dynamics of a silicon photonic crystal microcavity, Opt. Express **15**, 10294 (2007).

[26] A. Fang, T. Koschny, and C. M. Soukoulis, Lasing in metamaterial nanostructures, J. Opt. **12**, 024013 (2010).

[27] C. Fietz and C. M. Soukoulis, Finite element simulation of microphotonic lasing system, Opt. Express **20**, 11548 (2012).

[28] I. Prieto, J. M. Llorens, L. E. Muñoz-Camúñez, A. G. Taboada, J. Canet-Ferrer, J. M. Ripalda, C. Robles, G. Muñoz-Matutano, J. P. Martínez-Pastor, and P. A. Postigo, Near thresholdless laser operation at room temperature, Optica **2**, 66 (2015).

[29] H. Altug and J. Vučković, Photonic crystal nanocavity array laser, Opt. Express **13**, 8819 (2005).

[30] D. Bimberg and U. W. Pohl, Quantum dots: Promises and accomplishments, Mater. Today **14**, 388 (2011).

[31] A. Schliwa, G. Hönig, and D. Bimberg, Electronic properties of iii-v quantum dots, *Multi-Band Effective Mass Approximations* (Springer, Berlin, 2014), pp. 57–85.

[32] A. Markus, J. X. Chen, C. Paranthoen, A. Fiore, C. Platz, and O. Gauthier-Lafaye, Simultaneous two-state lasing in quantum-dot lasers, Appl. Phys. Lett. **82**, 1818 (2003).

[33] P. Borri, W. Langbein, S. Schneider, U. Woggon, R. L. Sellin, D. Ouyang, and D. Bimberg, Ultralong Dephasing Time in Ingaas Quantum Dots, Phys. Rev. Lett. **87**, 157401 (2001).

[34] T. H. Stievater, X. Li, D. G. Steel, D. Gammon, D. S. Katzer, D. Park, C. Piermarocchi, and L. J. Sham, Rabi Oscillations of Excitons in Single Quantum Dots, Phys. Rev. Lett. **87**, 133603 (2001).

[35] A. Zrenner, E. Beham, S. Stufler, F. Findeis, M. Bichler, and G. Abstreiter, Coherent properties of a two-level system based on a quantum-dot photodiode, Nature (London) **418**, 612 (2002).

[36] J. P. Reithmaier, G. Skek, A. Löffler, C. Hofmann, S. Kuhn, S. Reitzenstein, L. V. Keldysh, V. D. Kulakovskii, T. L. Reinecke, and A. Forchel, Strong coupling in a single quantum dot–semiconductor microcavity system, Nature (London) **432**, 197 (2004).

[37] B. Bidégaray, Time discretizations for Maxwell-Bloch equations, Numer. Methods Partial Different. Equations **19**, 284 (2003).

[38] W. Forysiak, R. G. Flesch, J. V. Moloney, and E. M. Wright, Doppler Shift of Self-Reflected Optical Pulses at an Interface: Dynamic Nonlinear Optical Skin Effect, Phys. Rev. Lett. **76**, 3695 (1996).

[39] S. Hughes, Breakdown of the Area Theorem: Carrier-Wave Rabi Flopping of Femtosecond Optical Pulses, Phys. Rev. Lett. **81**, 3363 (1998).

[40] O. D. Mücke, T. Tritschler, M. Wegener, U. Morgner, and F. X. Kärtner, Signatures of Carrier-Wave Rabi Flopping in Gaas, Phys. Rev. Lett. **87**, 057401 (2001).

[41] H. Takeda and S. John, Self-consistent maxwell-bloch theory of quantum-dot-population switching in photonic crystals, Phys. Rev. A **83**, 053811 (2011).

[42] R. W. Ziolkowski, J. M. Arnold, and D. M. Gogny, Ultrafast pulse interactions with two-level atoms, Phys. Rev. A **52**, 3082 (1995).

[43] G. Slavcheva, J. M. Arnold, I. Wallace, and R. W. Ziolkowski, Coupled Maxwell-pseudospin equations for investigation of self-induced transparency effects in a degenerate three-level quantum system in two dimensions: Finite-difference time-domain study, Phys. Rev. A **66**, 063418 (2002).

[44] J. Andreasen and H. Cao, Finite-difference time-domain formulation of stochastic noise in macroscopic atomic systems, J. Lightwave Technol. **27**, 4530 (2009).

[45] J. Andreasen, H. Cao, A. Taflove, P. Kumar, and Chang-qi Cao, Finite-difference time-domain simulation of thermal noise in open cavities, Phys. Rev. A **77**, 023810 (2008).

[46] M. Sukharev, Control of optical properties of hybrid materials with chirped femtosecond laser pulses under strong coupling conditions, J. Chem. Phys. **141**, 084712 (2014).

[47] M. Sukharev and A. Nitzan, Numerical studies of the interaction of an atomic sample with the electromagnetic field in two dimensions, Phys. Rev. A **84**, 043802 (2011).

[48] A. Pusch, S. Wuestner, J. M. Hamm, K. L. Tsakmakidis, and O. Hess, Coherent amplification and noise in gain-enhanced nanoplasmonic metamaterials: A Maxwell-Bloch Langevin approach, ACS Nano **6**, 2420 (2012).

[49] K. Lopata and D. Neuhausera, Nonlinear nanopolaritonics: Finite-difference time-domain maxwell-schrdinger simulation of molecule-assisted plasmon transfer, J. Chem. Phys. **131**, 014701 (2009).

[50] S. K. Gray and T. Kupka, Propagation of light in metallic nanowire arrays: Finite-difference time-domain studies of silver cylinders, Phys. Rev. B **68**, 045415 (2003).

[51] M. Dridi and G. C. Schatz, Model for describing plasmon-enhanced lasers that combines rate equations with finite-difference time-domain, J. Chem. Phys. **107**, 2791 (2009).

[52] S. Hughes, L. Ramunno, J. F. Young, and J. E. Sipe, Extrinsic Optical Scattering Loss in Photonic Crystal Waveguides: Role of Fabrication Disorder and Photon Group Velocity, Phys. Rev. Lett. **94**, 033903 (2005).

[53] M. Patterson, S. Hughes, S. Combrié, N.-V.-Quynh Tran, A. De Rossi, R. Gabet, and Y. Jaouën, Disorder-Induced Coherent Scattering in Slow-Light Photonic Crystal Waveguides, Phys. Rev. Lett. **102**, 253903 (2009); S. Mazoyer, J.-P. Hugonin, and P. Lalanne, Disorder-Induced Multiple Scattering in Photonic-Crystal Waveguides, *ibid.* **103**, 063903 (2009).

[54] M. Patterson, S. Hughes, S. Schulz, D. M. Beggs, T. P. White, L. OFaolain, and T. F. Krauss, Disorder-induced incoherent scattering losses in photonic crystal waveguides: Bloch mode reshaping, multiple scattering, and breakdown of the beer-lambert law, Phys. Rev. B **80**, 195305 (2009).

[55] N. L. Thomas, H. Zhang, J. Jágerská, V. Zabelin, R. Houdré, I. Sagnes, and A. Talneau, Light transport regimes in slow light photonic crystal waveguides, Phys. Rev. B **80**, 125332 (2009).

[56] L. Sapienza, H. Thyrrestrup, S. Stobbe, P. D. Garcia, S. Smolka, and P. Lodahl, Cavity quantum electrodynamics with anderson-localized modes, Science **327**, 1352 (2010).

[57] L. O'Faolain, S. A. Schulz, D. M. Beggs, T. P. White, M. Spasenović, L. Kuipers, F. Morichetti, A. Melloni, S. Mazoyer, J.-P. Hugonin *et al.*, Loss engineered slow light waveguides, Opt. Express **18**, 27627 (2010).

[58] J. Liu, P. D. Garcia, S. Ek, N. Gregersen, T. Suhr, M. Schubert, J. Mørk, S. Stobbe, and P. Lodahl, Random nanolasing in the anderson localized regime, Nat. Nanotechnol. **9**, 285 (2014).

[59] P. W. Anderson, Absence of diffusion in certain random lattices, Phys. Rev. **109**, 1492 (1958).

[60] F. A. Pinheiro, M. Rusek, A. Orlowski, and B. A. van Tiggelen, Probing anderson localization of light via decay rate statistics, Phys. Rev. E **69**, 026605 (2004).

[61] V. M. Apalkov and M. E. Raikh, Universal fluctuations of the random lasing threshold in a sample of a finite area, Phys. Rev. B **71**, 054203 (2005).

[62] P. Sebbah and C. Vanneste, Random laser in the localized regime, Phys. Rev. B **66**, 144202 (2002).

[63] J. P. Vasco and S. Hughes, Statistics of anderson-localized modes in disordered photonic crystal slab waveguides, Phys. Rev. B **95**, 224202 (2017).

[64] N. Gregersen, T. Suhr, M. Lorke, and J. Mørk, Quantum-dot nano-cavity lasers with purcell-enhanced stimulated emission, Appl. Phys. Lett. **100**, 131107 (2012).

[65] www.lumerical.com

[66] R.-C. Ge, P. T. Kristensen, J. F. Young, and S. Hughes, Quasinormal mode approach to modeling light-emission and propagation in nanoplasmonics, New J. Phys. **16**, 113048 (2014).

[67] P. T. Kristensen, C. V. Vlack, and S. Hughes, Generalized effective mode volume for leaky optical cavities, Opt. Lett. **37**, 1649 (2012).

[68] P. T. Kristensen, R.-C. Ge, and S. Hughes, Normalization of quasinormal modes in leaky optical cavities and plasmonic resonators, Phys. Rev. A **92**, 053810 (2015).

[69] P. Yao, V. S. C. M. Rao, and S. Hughes, On-chip single photon sources using planar photonic crystals and single quantum dots, Laser Photon. Rev. **4**, 499 (2010).

[70] N. Mann, A. Javadi, P. D. García, P. Lodahl, and S. Hughes, Theory and experiments of disorder-induced resonance shifts and mode-edge broadening in deliberately disordered photonic crystal waveguides, Phys. Rev. A **92**, 023849 (2015).

[71] M. Minkov, U. P. Dharanipathy, R. Houdré, and V. Savona, Statistics of the disorder-induced losses of high-q photonic crystal cavities, Opt. Express **21**, 28233 (2013).

[72] E. S. Semenova, I. V. Kulkova, S. Kadkhodazadeh, D. Barettin, O. Kopylov, A. Cagliani, K. Almdal, M. Willatzen, and K. Yvind, Epitaxial growth of quantum dots on inp for device applications operating at the 1.55 μm wavelength range, *SPIE OPTO* (SPIE-International Society for Optics and Photonics, Bellingham, WA, 2014), pp. 899606–899606.

[73] A. Moelbjerg, P. Kaer, M. Lorke, B. Tromborg, and J. Mørk, Dynamical properties of nanolasers based on few discrete emitters, IEEE J. Quantum Electron. **49**, 945 (2013).

[74] J. L. Skinner and D. Hsu, Pure dephasing of a two-level system, J. Phys. Chem. **90**, 4931 (1986).

[75] V. S. C. M. Rao and S. Hughes, Single quantum-dot purcell factor and β factor in a photonic crystal waveguide, Phys. Rev. B **75**, 205437 (2007).

[76] E. Schelew, G. Rong-Chung, S. Hughes, J. Pond, and J. F. Young, Self-consistent numerical modeling of radiatively damped Lorentz oscillators, Phys. Rev. A **95**, 063853 (2017).

[77] P. W. Milonni and J. H. Eberly, Laser Physics (to be published).

[78] L. Allen and J. H Eberly, Optical resonance and two-level atoms, Courier Corporation (2012), https://www.amazon.com/Optical-Resonance-Two-Level-Atoms-Physics/dp/0486655334.

[79] http://www.lumerical.com/tcad-products/fdtd/, Lumerical Solutions, inc.

[80] S. Stobbe, P. T. Kristensen, J. E. Mortensen, J. M. Hvam, J. Mørk, and P. Lodahl, Spontaneous emission from large quantum dots in nanostructures: Exciton-photon interaction beyond the dipole approximation, Phys. Rev. B **86**, 085304 (2012).

[81] S. Stobbe, J. M. Hvam, and P. Lodahl, On the interpretation of wave function overlaps in quantum dots, Phys. Status Solidi B **248**, 855 (2011).

[82] E. Rosencher and B. Vinter, *Optoelectronics* (Cambridge University Press, Cambridge, 2002).

[83] L. C. Andreani, G. Panzarini, and J.-M. Gérard, Strong-coupling regime for quantum boxes in pillar microcavities: Theory, Phys. Rev. B **60**, 13276 (1999).

[84] L. Novotny and B. Hecht, *Principles of Nano-optics* (Cambridge University Press, Cambridge, 2012).

[85] O. J. F. Martin and N. B. Piller, Electromagnetic scattering in polarizable backgrounds, Phys. Rev. E **58**, 3909 (1998).

[86] P. T. Kristensen, J. Mørk, P. Lodahl, and S. Hughes, Decay dynamics of radiatively coupled quantum dots in photonic crystal slabs, Phys. Rev. B **83**, 075305 (2011).

[87] G. S. Agarwal, *Quantum Optics* (Cambridge University Press, Cambridge, 2013).

[88] H. A. M. Leymann, A. Foerster, F. Jahnke, J. Wiersig, and C. Gies, Sub-and Superradiance in Nanolasers, Phys. Rev. Appl. **4**, 044018 (2015).

[89] S. Hughes and H. Kamada, Single-quantum-dot strong coupling in a semiconductor photonic crystal nanocavity side coupled to a waveguide, Phys. Rev. B **70**, 195313 (2004).

[90] R. Faggiani, A. Baron, X. Zang, L. Lalouat, S. A. Schulz, B. O'Regan, K. Vynck, B. Cluzel, F. D. Fornel, T. F. Krauss *et al.*, Lower bound for the spatial extent of localized modes in photonic-crystal waveguides with small random imperfections, Sci. Rep. **6**, 27037 (2016).

[91] S. Ek, P. Lunnemann, E. Semenova, K. Yvind, and J. Mørk, Slow-light-enhanced gain in active photonic crystal waveguides, Nat. Commun. **5**, 5039 (2014).